

# Observability-Enhancement Boresight Calibration of Camera-IMU System: Theory and Experiments

Xiwen Yang<sup>†</sup>, Ziheng Cheng<sup>†</sup> and Shaoming He<sup>\*</sup>

**Abstract**—Airborne target tracking with vision sensors is one of the indispensable and critical components in unmanned aerial vehicles (UAVs). It is critical to calibrate the misalignment angles between the onboard camera and Inertial Measurement Unit (IMU) to improve the accuracy of target tracking. In this paper, the observability of boresight misalignment angle estimation using a cooperative target is first analyzed. Based on the observability Gramian, an optimization criterion for maximizing the degree of observability is determined, and the optimal geometries between the UAV and the target are derived. Taking the physical constraints of the UAV into consideration, an online trajectory optimization approach for a UAV with a vision sensor is proposed to achieve in-flight calibration of the misalignment angles. Both numerical simulations and experiments are conducted to validate the proposed method.

**Index Terms**—Boresight calibration, Camera-IMU system, Observability analysis, Configuration optimization

## I. INTRODUCTION

Autonomous target tracking is an essential task for UAVs in a wide variety of applications, including surveillance [1], environment monitoring [2], traffic management [3], and search and rescue [4]. Thanks to the progress in computer vision, image-based airborne target tracking methods have achieved an exceptional level of performance on real-world small-scale UAVs in recent years [5], [6]. These methods heavily rely on accurate integration of the onboard IMU and the camera measurements since the bearing information extracted from the received image is with respect to the UAV body frame [7], yet most works explicitly assume that the gimbal/camera frame and the UAV body frame are perfectly aligned and collocated [8]–[11]. However, there inevitably exists boresight misalignment angle between these two frames due to improper installations. This misalignment error is shown to significantly degrade the tracking performance if not properly calibrated, and hence boresight calibration of a camera-IMU system becomes a fundamental requirement for vision-based airborne target tracking.

The calibration of sensor bias, such as additive and multiplicative errors, has been widely studied in existing target tracking works [12]–[14]. With the assumption that the altitude of the target is known a priori, the horizontal position of the target and an additive constant bias in the aircraft heading angle are jointly estimated using linear regression method [15]. The two-dimensional target tracking problem with a

sensor bias in bearing measurements is studied in [16], and the angle bias is also jointly estimated with the position of a stationary target using Kalman filter (KF). By combining the sensor registration and track-to-track fusion process in multi-target tracking, the influence of additive biases in bearing measurements is mitigated under the condition that at least one target is visible to both of the two radars [17]. Augmenting the navigation and gimbal biases in the system states, the authors in [18] proposed a decentralized algorithm to estimate the unknown target state and the sensor biases in an integrated manner using extended information filter (EIF). The result shows that with a target-centered trajectory, the biases in UAV attitude and camera gimbal cannot be jointly estimated due to poor system observability. For the multi-sensor multi-target tracking scenarios considered in [19], the range and azimuth measurements are modeled to be corrupted by both scaling and offset biases, which are estimated from pseudo-measurements calculated by the target state estimates in local trackers. However, these sensor models only considered additive and/or multiplicative errors, which are not suitable for boresight misalignment angle estimation.

Unlike sensor biases, the calibration of boresight misalignment angles involves estimating the rotational relationship between camera and IMU frames. This relationship cannot be modeled as either offset or scaling biases in the sensor output. The boresight or the physical mounting angle calibration problem in integrated camera-IMU systems has been frequently investigated in the field of airborne mapping and navigation [20]–[24]. A conventional solution to this problem is to first collect images from a calibration site with a certain number of well-distributed known ground control points (GCPs), and then determine the boresight matrix using the bundle adjustment approach [20], [25], [26]. The authors in [24] calibrated the lever arms and boresight misalignment of an integrated navigation system in a standard test field with over 200 GCPs. In [27], the methods based on GCPs and tie features for boresight calibration between the hyper-spectral scanner and navigation system on a UAV platform were proposed. The deficiency of this conventional calibration method lies in that it is impractical to implement a GCP network in some inaccessible field environments. Therefore, investigating boresight calibration methods without GCPs is more meaningful in terms of real applications. In [28] and [29], the misalignment angles between the camera and IMU are estimated by combining adjustment between the images and point clouds generated by an extra onboard LIDAR system, which is inapplicable for small-scale UAVs due to limited computational power. The authors in [30]–[33] determined the IMU-camera extrinsic

Xiwen Yang, Ziheng Cheng and Shaoming He are with the School of Aerospace Engineering, Beijing Institute of Technology, Beijing 100081, China

<sup>†</sup>These authors contributed equally.

<sup>\*</sup>Corresponding Author. Email: shaoming.he@bit.edu.cn

parameters and the biases of IMU components in the vision-aided inertial navigation systems (VINS) by augmenting the navigation state vector. The primary issue associated with existing boresight calibration methods is that they fail to analyze the degree of observability of the problem at hand. Generally, the quality of sensor calibration is proportional to the degree of system observability, and therefore actively optimizing the system observability is the key enabler to realize in-flight boresight calibration.

Driven by the aforementioned challenges, the purpose of this paper is to present a simple yet efficient boresight calibration approach for the integrated camera-IMU systems. Based on the observability Gramian, we first analyze the observability of boresight estimation using a cooperative target with rigorous mathematical derivations. The UAV-target configuration is then optimized by maximizing the determinant of the observability Gramian and some special cases are presented to provide better insights of the optimal relative geometry. An online two-dimensional UAV trajectory optimization approach with physical constraints is proposed to complete the calibration process. Since the target position in body frame is determined by both the attitude and position of the UAV, the dynamic model of a quadrotor is employed and a multi-step optimization strategy is applied in the development of the trajectory planning approach. Numerical simulations and in-door experiments are finally conducted to evaluate the performance of the proposed algorithm.

The contributions of this paper are two folds. On one hand, it is found that the degree of observability in misalignment angle calibration is related to the relative positions of the cooperative target in the UAV body frame. This reveals that the calibration performance is determined by both the attitude and position of the UAV, and is the key foundation to find an observability-enhancement optimal UAV-target configuration in the body frame. Up to the best of our knowledge, this problem has not been analyzed before in the literature. On the other hand, a trajectory optimization approach for in-flight camera-IMU calibration is proposed with both numerical and experimental validations. Compared to the non-optimized UAV trajectories, the experimental results clearly show that the calibration performance is improved by the proposed approach.

The remainder of this paper is organized as follows. Sec. II provides some preliminaries and formulates the problem. Sec. III analyzes the observability of the boresight calibration system. The optimal UAV-target configuration is then given in Sec. IV through numerical studies. In Sec. V, the online trajectory optimization method for observability-enhancement calibration is presented, followed by the simulation and experiment results in Sec. VI. Finally, the pertinent conclusions are drawn in Sec. VII.

## II. PRELIMINARIES AND PROBLEM FORMULATION

This section illustrates the geometric relationship between the UAV and the cooperative target considering camera-IMU misalignment. Then, the observability Gramian is briefly reviewed to facilitate the following analysis and the problem formulation of this work is also stated.

### A. Geometry of Vision-Based Target Localization

The geometry of target localization using UAV platform with a gimballed camera is illustrated in Fig. 1, where  $O_n - X_n Y_n Z_n$  and  $O - X_b Y_b Z_b$  represent the local north-east-down (NED) frame and the body frame of the UAV, respectively. The notations  $\mathbf{P}^t = [x_n^t, y_n^t, z_n^t]^T$  and  $\mathbf{P}^u = [x_n^u, y_n^u, z_n^u]^T$  are the position vectors of the target and UAV in the inertial coordinate, respectively. The coordinates of the cooperative target in UAV body frame are given by

$$\begin{bmatrix} x_b \\ y_b \\ z_b \end{bmatrix} = C_n^b \begin{bmatrix} x_n^t - x_n^u \\ y_n^t - y_n^u \\ z_n^t - z_n^u \end{bmatrix} \quad (1)$$

where  $C_n^b$  is the rotation matrix from the local NED frame to the body frame, given by

$$C_n^b = \begin{bmatrix} C_\psi C_\theta & S_\psi C_\theta & -S_\theta \\ C_\psi S_\theta S_\phi - S_\psi C_\phi & S_\psi S_\theta S_\phi + C_\psi C_\phi & C_\theta S_\phi \\ C_\psi S_\theta C_\phi + S_\psi S_\phi & S_\psi S_\theta C_\phi - C_\psi S_\phi & C_\theta C_\phi \end{bmatrix} \quad (2)$$

with  $\phi, \theta, \psi$  representing the roll, pitch, and yaw angles of the UAV,  $C_{(\cdot)}$  and  $S_{(\cdot)}$  representing  $\cos(\cdot)$  and  $\sin(\cdot)$ , respectively.

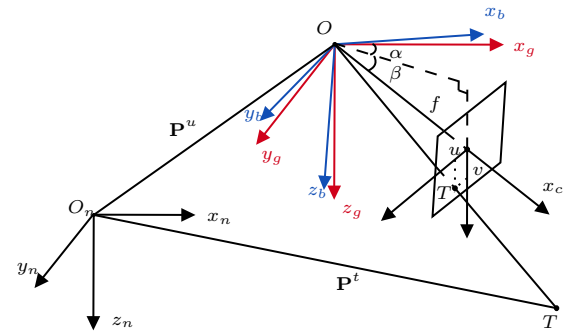


Fig. 1. Geometry of vision-based target localization using UAV platform

In Fig. 1,  $u$  and  $v$  are the pixel coordinates of the cooperative target  $T$  in the focal plane, which can be obtained from the gimballed camera. Denote the camera reference frame as  $O - X_c Y_c Z_c$ , whose origin is translated to that of the body frame. Based on a simple pinhole camera model, the target position vector in camera frame can be readily obtained as

$$\begin{bmatrix} x_c \\ y_c \\ z_c \end{bmatrix} = \frac{\|\mathbf{P}^t - \mathbf{P}^u\|}{\sqrt{u^2 + v^2 + f^2}} \begin{bmatrix} f \\ u \\ v \end{bmatrix} \quad (3)$$

where  $f$  is the focal length of the camera.

Let  $\alpha$  and  $\beta$  represent the azimuth and elevation angles of the camera relative to the gimbal base frame, i.e.,  $O - X_g Y_g Z_g$  in Fig. 1. Then, the following equation holds,

$$\begin{bmatrix} x_g \\ y_g \\ z_g \end{bmatrix} = C_c^g \begin{bmatrix} x_c \\ y_c \\ z_c \end{bmatrix} \quad (4)$$

where  $C_c^g$  is the rotation matrix from the camera frame to the gimbal base frame as

$$C_c^g = \begin{bmatrix} C(\alpha)C(\beta) & -S(\alpha) & C(\alpha)S(\beta) \\ S(\alpha)S(\beta) & C(\alpha) & S(\alpha)S(\beta) \\ -S(\beta) & 0 & C(\beta) \end{bmatrix} \quad (5)$$

From Eqs. (1) and (4), we obtain the coordinate of the cooperative target in the UAV body frame and the gimbal base frame. However, the body frame determined by the on-board IMU sensor is usually misaligned with the gimbal base frame due to the existence of mounting errors. Denoting the constant misalignment angles by  $e_x, e_y, e_z$ , the relationship between the target position vectors in these two frames is expressed as

$$\begin{bmatrix} x_g \\ y_g \\ z_g \end{bmatrix} = C_b^g \begin{bmatrix} x_b \\ y_b \\ z_b \end{bmatrix} \quad (6)$$

where  $C_b^g$  is the rotation matrix from body frame to gimbal base frame, given by

$$C_b^g = \begin{bmatrix} C_{e_z} C_{e_y} & S_{e_z} C_{e_y} & -S_{e_y} \\ C_{e_z} S_{e_y} S_{e_x} - S_{e_z} C_{e_x} & S_{e_z} S_{e_y} S_{e_x} + C_{e_z} C_{e_x} & C_{e_y} S_{e_x} \\ C_{e_z} S_{e_y} C_{e_x} + S_{e_z} S_{e_x} & S_{e_x} S_{e_y} C_{e_x} - C_{e_z} S_{e_x} & C_{e_y} C_{e_x} \end{bmatrix} \quad (7)$$

Assume that the misalignment errors  $e_x, e_y, e_z$  are small angles, Eq. (7) can be reduced to

$$C_b^g = \begin{bmatrix} 1 & e_z & -e_y \\ -e_z & 1 & e_x \\ e_y & -e_x & 1 \end{bmatrix} \quad (8)$$

Combining Eqs. (6) and (8), a linear measurement function of the misalignment angles is obtained as

$$\begin{bmatrix} x_g - x_b \\ y_g - y_b \\ z_g - z_b \end{bmatrix} = \begin{bmatrix} 0 & -z_b & y_b \\ z_b & 0 & -x_b \\ -y_b & x_b & 0 \end{bmatrix} \begin{bmatrix} e_x \\ e_y \\ e_z \end{bmatrix} \quad (9)$$

### B. Observability Gramian

Consider a discrete-time linear system described by equations of the form

$$\begin{aligned} \mathbf{x}_{k+1} &= \mathbf{F}_k \mathbf{x}_k \\ \mathbf{y}_k &= \mathbf{H}_k \mathbf{x}_k \end{aligned} \quad (10)$$

where  $\mathbf{x}_k \in \mathbb{R}^n$  denotes the system state vector at time  $t_k$  and  $\mathbf{y} \in \mathbb{R}^m$  represents the measurement vector. The matrices  $\mathbf{F}_k$  and  $\mathbf{H}_k$  stand for the system transition and measurement model, respectively.

The observability Gramian of system (10) at time step  $t_k$  is defined as [34]

$$\mathbf{W}_k = \mathcal{O}_k^T \mathcal{O}_k \quad (11)$$

where the observability matrix  $\mathcal{O}_k$  is determined by

$$\mathcal{O}_k = \begin{bmatrix} \mathbf{H}_1 \\ \mathbf{H}_2 \mathbf{F}_1 \\ \vdots \\ \mathbf{H}_k \mathbf{F}_{k-1} \cdots \mathbf{F}_1 \end{bmatrix} \quad (12)$$

According to [34], system (10) is observable if and only if  $\mathbf{W}_k$ , or equivalently,  $\mathcal{O}_k$  is full-rank. Therefore, the system is observable at time  $k$  if the following condition is satisfied

$$\det[\mathbf{W}_k] \neq 0 \quad (13)$$

### C. Problem Statement

To improve the accuracy and efficiency of boresight calibration, this work aims to analyze the observability of the misalignment angles and further actively optimize the relative configuration of UAV and the cooperative target.

## III. OBSERVABILITY ANALYSIS

Since the system observability is a key index of state estimation performance, the observability of boresight calibration problem is analyzed in this section.

### A. Observability Analysis of Boresight Calibration System

Let  $\mathbf{x} = [e_x, e_y, e_z]^T$  be the system state vector of the boresight calibration problem. Since the misalignment angles are assumed to be constant, the state transition matrix  $\mathbf{F}_k$  is given as

$$\mathbf{F}_k = \begin{bmatrix} 1 & 0 & 0 \\ 0 & 1 & 0 \\ 0 & 0 & 1 \end{bmatrix} \quad (14)$$

From Eq. (9), the measurement matrix at time  $t_k$  is given by

$$\mathbf{H}_k = \begin{bmatrix} 0 & -z_{b,k} & y_{b,k} \\ z_{b,k} & 0 & -x_{b,k} \\ -y_{b,k} & x_{b,k} & 0 \end{bmatrix} \quad (15)$$

where the subscript  $k$  is included in the coordinates expression to denote time step  $t_k$ .

Substituting Eqs. (14) and (15) into Eq. (11) yields the observability Gramian of the boresight calibration system as

$$\mathbf{W}_k = \sum_{i=1}^k \mathbf{H}_i^T \mathbf{H}_i = \begin{bmatrix} \sum_{i=1}^k \rho_{yz,i}^2 & -I_{z,k} & -I_{y,k} \\ -I_{z,k} & \sum_{i=1}^k \rho_{xz,i}^2 & -I_{x,k} \\ -I_{y,k} & -I_{x,k} & \sum_{i=1}^k \rho_{xy,i}^2 \end{bmatrix} \quad (16)$$

where the range-related and inertia-related terms are defined as

$$\begin{aligned} \rho_{xy,i} &= \sqrt{x_{b,i}^2 + y_{b,i}^2}, \quad \rho_{xz,i} = \sqrt{x_{b,i}^2 + z_{b,i}^2} \\ \rho_{yz,i} &= \sqrt{y_{b,i}^2 + z_{b,i}^2}, \quad I_{x,k} = \sum_{i=1}^k y_{b,i} z_{b,i} \\ I_{y,k} &= \sum_{i=1}^k x_{b,i} z_{b,i}, \quad I_{z,k} = \sum_{i=1}^k x_{b,i} y_{b,i} \end{aligned} \quad (17)$$

After some tedious but straightforward algebraic manipulations, it is easy to verify that  $\det(\mathbf{W}_1) = 0$ , which means the states are unobservable with only one-scan measurements. The determinant of the observability Gramian in case of  $k \geq 2$  is derived as

$$\begin{aligned} \det(\mathbf{W}_k) &= \sum_{i=1}^k \rho_{xy,i}^2 \left[ \sum_{i=1}^k \rho_{xz,i}^2 \sum_{i=1}^k \rho_{yz,i}^2 - (I_{z,k})^2 \right] - I_{x,k} \left[ I_{x,k} \sum_{i=1}^k \rho_{yz,i}^2 \right. \end{aligned}$$

$$\begin{aligned}
& + I_{z,k} I_{y,k} \Big] - I_{y,k} \left[ I_{x,k} I_{z,k} + I_{y,k} \sum_{i=1}^k \rho_{xz,i}^2 \right] \\
= & \left( \sum_{i=1}^k \rho_{xy,i}^2 \right)^2 \sum_{i=1}^k z_{b,i}^2 + \sum_{i=1}^k \rho_{xy,i}^2 \left( \sum_{i=1}^k z_{b,i}^2 \right)^2 \\
& + \sum_{i=1}^k \rho_{xy,i}^2 \sum_{i=1}^k x_{b,i}^2 \sum_{i=1}^k y_{b,i}^2 - (I_{z,k})^2 \sum_{i=1}^k \rho_{xy,i}^2 \\
& - (I_{x,k})^2 \sum_{i=1}^k \rho_{yz,i}^2 - (I_{y,k})^2 \sum_{i=1}^k \rho_{xz,i}^2 - 2I_{z,k} I_{y,k} I_{x,k} \\
= & \left[ \sum_{i=1}^k x_{b,i}^2 \sum_{i=1}^k z_{b,i}^2 \sum_{i=1}^k \rho_i^2 - (I_{y,k})^2 \sum_{i=1}^k \rho_{xz,i}^2 \right] \\
& + \left[ \sum_{i=1}^k y_{b,i}^2 \sum_{i=1}^k z_{b,i}^2 \sum_{i=1}^k \rho_i^2 - (I_{x,k})^2 \sum_{i=1}^k \rho_{yz,i}^2 \right] \\
& + \sum_{i=1}^k \rho_{xy,i}^2 \left[ \sum_{i=1}^k x_{b,i}^2 \sum_{i=1}^k y_{b,i}^2 - (I_{z,k})^2 \right] - 2I_{z,k} I_{y,k} I_{x,k}
\end{aligned} \tag{18}$$

where  $\rho_i$  stands for the distance between the UAV and the cooperative target at time  $t_i$ , i.e.,  $\rho_i = \sqrt{x_{b,i}^2 + y_{b,i}^2 + z_{b,i}^2}$ .

Rearranging terms in Eq. (18) yields

$$\begin{aligned}
\det(\mathbf{W}_k) & = \sum_{i=1}^k \rho_{xz,i}^2 \left[ \sum_{i=1}^k x_{b,i}^2 \sum_{i=1}^k z_{b,i}^2 - (I_{y,k})^2 \right] + \sum_{i=1}^k \rho_{yz,i}^2 \left[ \sum_{i=1}^k y_{b,i}^2 \sum_{i=1}^k z_{b,i}^2 - (I_{x,k})^2 \right] \\
& + \sum_{i=1}^k \rho_{xy,i}^2 \left[ \sum_{i=1}^k x_{b,i}^2 \sum_{i=1}^k y_{b,i}^2 - (I_{z,k})^2 \right] \\
& + 2 \sum_{i=1}^k x_{b,i}^2 \sum_{i=1}^k y_{b,i}^2 \sum_{i=1}^k z_{b,i}^2 - 2I_{z,k} I_{y,k} I_{x,k}
\end{aligned} \tag{19}$$

Notice that one can easily verify that

$$\begin{aligned}
& \sum_{i=1}^k x_{b,i}^2 \sum_{i=1}^k y_{b,i}^2 - \left( \sum_{i=1}^k x_{b,i} y_{b,i} \right)^2 \\
& = \sum_{1 \leq i < j \leq k} (x_{b,i} y_{b,j} - x_{b,j} y_{b,i})^2
\end{aligned} \tag{20}$$

Therefore, Eq. (19) is equivalent to the following form

$$\begin{aligned}
\det(\mathbf{W}_k) & = \sum_{i=1}^k \rho_{xz,i}^2 \sum_{1 \leq i < j \leq k} c_{xz,ij}^2 + \sum_{i=1}^k \rho_{yz,i}^2 \sum_{1 \leq i < j \leq k} c_{yz,ij}^2 + \sum_{i=1}^k \rho_{xy,i}^2 \\
& \times \sum_{1 \leq i < j \leq k} c_{xy,ij}^2 + 2 \underbrace{\sum_{i=1}^k x_{b,i}^2 \sum_{i=1}^k y_{b,i}^2 \sum_{i=1}^k z_{b,i}^2 - 2I_{z,k} I_{y,k} I_{x,k}}_{M_k}
\end{aligned} \tag{21}$$

where the cross-product terms are defined as

$$\begin{aligned}
c_{xy,ij} & = x_{b,i} y_{b,j} - x_{b,j} y_{b,i}, \quad c_{xz,ij} = x_{b,i} z_{b,j} - x_{b,j} z_{b,i}, \\
c_{yz,ij} & = y_{b,i} z_{b,j} - y_{b,j} z_{b,i}
\end{aligned} \tag{22}$$

Denote the latter part of Eq. (21) as  $M_k$ . In case of  $k = 2$ , we have Eq. (23) shown at the beginning of next page.

Hence, we have

$$\begin{aligned}
\det(\mathbf{W}_2) & = (x_{b,1}^2 + x_{b,2}^2 + z_{b,1}^2 + z_{b,2}^2) c_{xz,12}^2 + (y_{b,1}^2 + y_{b,2}^2 + z_{b,1}^2 \\
& + z_{b,2}^2) c_{yz,12}^2 + (x_{b,1}^2 + x_{b,2}^2 + y_{b,1}^2 + y_{b,2}^2) c_{xy,12}^2 + M_2 \\
& = \sum_{i=1}^2 (x_{b,i}^2 + y_{b,i}^2 + z_{b,i}^2) (c_{xy,12}^2 + c_{xz,12}^2 + c_{yz,12}^2) \\
& = \sum_{i=1}^2 \rho_i^2 \|\mathbf{P}_{b,1} \times \mathbf{P}_{b,2}\|^2
\end{aligned} \tag{24}$$

where  $\mathbf{P}_{b,i} = [x_{b,i}, y_{b,i}, z_{b,i}]^T$  represents the position vector of the target in the UAV body frame at time  $t_i$ .

If  $k \geq 3$ ,  $M_k$  can be rewritten as Eq. (25). Then,  $\det(\mathbf{W}_k)$  is derived as Eq. (26). Combing Eqs. (24) and (26) yields Eq. (27).

**Proposition 1.** *The boresight calibration system is unobservable if the target position vectors projected into the UAV body frame at sampling time instants  $t_1, t_2, \dots, t_k$  are collinear.*

*Proof.* We prove Proposition 1 by an intuitive geometric interpretation of Eq. (27). As depicted in Fig. 2, the term  $\|\mathbf{P}_{b,i} \times \mathbf{P}_{b,j}\|$  represents the area of the parallelogram formed by vectors  $\mathbf{P}_{b,i}$  and  $\mathbf{P}_{b,j}$ , while the absolute value of the mixed product  $(\mathbf{P}_{b,i} \times \mathbf{P}_{b,j}) \cdot \mathbf{P}_{b,m}$  gives the volume of parallelepiped constructed by the three vectors involved.

If the vectors  $\mathbf{P}_{b,1}, \mathbf{P}_{b,2}, \dots, \mathbf{P}_{b,k}$  are collinear with each other, it is obvious that Eq. (27) equals zero since the areas of parallelograms and the volumes of the parallelepipeds formed by these vectors are zero. This means the system is unobservable under this condition.  $\square$

#### IV. OPTIMIZATION OF UAV-TARGET CONFIGURATION

Note that the check on the rank of observability Gramian only gives an answer to the binary problem of whether the system is observable or not. In order to determine the optimal set of observations and improve the estimation performance, this section determines an optimization criterion to measure the degree of observability of the boresight calibration system. Further, the optimal geometries and numerical results in some special cases are analyzed.

##### A. Selection of Optimality Metric

According to [35], matrix measures of the observability Gramian can reflect the quality of system observability. However, finding the optimal relative geometry requires a scalar metric. The most common scalable function of a matrix include the trace, the smallest eigenvalue and the determinant of the matrix. From Eq. (16), the trace of observability Gramian  $\mathbf{W}_k$  is given by

$$\text{tr}(\mathbf{W}_k) = \sum_{i=1}^k (\rho_{xy,i}^2 + \rho_{xz,i}^2 + \rho_{yz,i}^2) = 2 \sum_{i=1}^k \rho_i^2 \tag{28}$$

$$\begin{aligned}
 M_2 &= 2(x_{b,1}^2 + x_{b,2}^2)(y_{b,1}^2 + y_{b,2}^2)(z_{b,1}^2 + z_{b,2}^2) - 2(x_{b,1}y_{b,1} + x_{b,2}y_{b,2})(x_{b,1}z_{b,1} + x_{b,2}z_{b,2})(y_{b,1}z_{b,1} + y_{b,2}z_{b,2}) \\
 &= (x_{b,1}y_{b,2}z_{b,1} - x_{b,2}y_{b,1}z_{b,1})^2 + (x_{b,1}y_{b,2}z_{b,1} - x_{b,1}y_{b,1}z_{b,2})^2 + (x_{b,2}y_{b,1}z_{b,1} - x_{b,1}y_{b,1}z_{b,2})^2 \\
 &\quad + (x_{b,2}y_{b,2}z_{b,1} - x_{b,2}y_{b,1}z_{b,2})^2 + (x_{b,2}y_{b,2}z_{b,1} - x_{b,1}y_{b,2}z_{b,2})^2 + (x_{b,1}y_{b,2}z_{b,2} - x_{b,2}y_{b,1}z_{b,2})^2 \\
 &= (z_{b,1}^2 + z_{b,2}^2)c_{xy,12}^2 + (y_{b,1}^2 + y_{b,2}^2)c_{xz,12}^2 + (x_{b,1}^2 + x_{b,2}^2)c_{yz,12}^2
 \end{aligned} \tag{23}$$

$$\begin{aligned}
 M_k &= \sum_{1 \leq i < j \leq k} [(z_{b,i}^2 + z_{b,j}^2)c_{xy,ij}^2 + (y_{b,i}^2 + y_{b,j}^2)c_{xz,ij}^2 + (x_{b,i}^2 + x_{b,j}^2)c_{yz,ij}^2] + \sum_{1 \leq i < j < m \leq k} [(x_{b,i}y_{b,j}z_{b,m} - x_{b,m}y_{b,i}z_{b,j})^2 \\
 &\quad + (x_{b,m}y_{b,i}z_{b,j} - x_{b,j}y_{b,m}z_{b,i})^2 + (x_{b,j}y_{b,m}z_{b,i} - x_{b,i}y_{b,j}z_{b,m})^2 + (x_{b,m}y_{b,j}z_{b,i} - x_{b,i}y_{b,m}z_{b,j})^2 \\
 &\quad + (x_{b,i}y_{b,m}z_{b,j} - x_{b,j}y_{b,i}z_{b,m})^2 + (x_{b,j}y_{b,i}z_{b,m} - x_{b,m}y_{b,j}z_{b,i})^2]
 \end{aligned} \tag{25}$$

$$\begin{aligned}
 \det(\mathbf{W}_k) &= \sum_{i=1}^k \rho_{xz,i}^2 \sum_{1 \leq i < j \leq k} c_{xz,ij}^2 + \sum_{i=1}^k \rho_{yz,i}^2 \sum_{1 \leq i < j \leq k} c_{yz,ij}^2 + \sum_{i=1}^k \rho_{xy,i}^2 \sum_{1 \leq i < j \leq k} c_{xy,ij}^2 + M_k \\
 &= \sum_{1 \leq i < j \leq k} \left[ \left( \sum_{l=1}^k \rho_l^2 - \sum_{l=1, l \neq i, j}^k z_{b,l}^2 \right) c_{xy,ij}^2 + \left( \sum_{l=1}^k \rho_l^2 - \sum_{l=1, l \neq i, j}^k y_{b,l}^2 \right) c_{xz,ij}^2 \right. \\
 &\quad \left. + \left( \sum_{l=1}^k \rho_l^2 - \sum_{l=1, l \neq i, j}^k x_{b,l}^2 \right) c_{yz,ij}^2 \right] + \sum_{1 \leq i < j < m \leq k} [(x_{b,i}y_{b,j}z_{b,m} - x_{b,m}y_{b,i}z_{b,j})^2 \\
 &\quad + (x_{b,m}y_{b,i}z_{b,j} - x_{b,j}y_{b,m}z_{b,i})^2 + (x_{b,j}y_{b,m}z_{b,i} - x_{b,i}y_{b,j}z_{b,m})^2 + (x_{b,m}y_{b,j}z_{b,i} - x_{b,i}y_{b,m}z_{b,j})^2 \\
 &\quad + (x_{b,i}y_{b,m}z_{b,j} - x_{b,j}y_{b,i}z_{b,m})^2 + (x_{b,j}y_{b,i}z_{b,m} - x_{b,m}y_{b,j}z_{b,i})^2] \\
 &= \sum_{l=1}^k \rho_l^2 \sum_{1 \leq i < j \leq k} (c_{xy,ij}^2 + c_{xz,ij}^2 + c_{yz,ij}^2) + \sum_{1 \leq i < j < m \leq k} [(x_{b,i}y_{b,j}z_{b,m} - x_{b,m}y_{b,i}z_{b,j})^2 \\
 &\quad + (x_{b,m}y_{b,i}z_{b,j} - x_{b,j}y_{b,m}z_{b,i})^2 + (x_{b,j}y_{b,m}z_{b,i} - x_{b,i}y_{b,j}z_{b,m})^2 + (x_{b,m}y_{b,j}z_{b,i} - x_{b,i}y_{b,m}z_{b,j})^2 \\
 &\quad + (x_{b,i}y_{b,m}z_{b,j} - x_{b,j}y_{b,i}z_{b,m})^2 + (x_{b,j}y_{b,i}z_{b,m} - x_{b,m}y_{b,j}z_{b,i})^2 - (z_{b,i}^2 c_{xy,jm}^2 + y_{b,i}^2 c_{xz,jm}^2 + x_{b,i}^2 c_{yz,jm}^2) \\
 &\quad - (z_{b,j}^2 c_{xy,im}^2 + y_{b,j}^2 c_{xz,im}^2 + x_{b,j}^2 c_{yz,im}^2) - (z_{b,m}^2 c_{xy,ij}^2 + y_{b,m}^2 c_{xz,ij}^2 + x_{b,m}^2 c_{yz,ij}^2)] \\
 &= \sum_{l=1}^k \rho_l^2 \sum_{1 \leq i < j \leq k} (c_{xy,ij}^2 + c_{xz,ij}^2 + c_{yz,ij}^2) - \sum_{1 \leq i < j < m \leq k} (x_{b,m}c_{yz,ij} - y_{b,m}c_{xz,ij} + z_{b,m}c_{xy,ij})^2 \\
 &= \sum_{i=1}^k \rho_i^2 \sum_{1 \leq i < j \leq k} \|\mathbf{P}_{b,i} \times \mathbf{P}_{b,j}\|^2 - \sum_{1 \leq i < j < m \leq k} [(\mathbf{P}_{b,i} \times \mathbf{P}_{b,j}) \cdot \mathbf{P}_{b,m}]^2
 \end{aligned} \tag{26}$$

which reveals that maximizing the trace of  $\mathbf{W}_k$  tends to increase the range between the UAV and the cooperative target. Obviously, this is not a proper objective function for configuration optimization since the angular information is ignored. This means a set of collinear relative position vectors can also yield a large value of  $\text{tr}(\mathbf{W}_k)$ , resulting in an unobservable estimation.

Since the determinant contains information of all elements of a matrix and represents the observability of all dimensions equally, the determinant of  $\mathbf{W}_k$  is chosen over the smallest eigenvalue to serve as the optimization criterion. Therefore, the UAV-target configuration optimization problem can be described as

$$\max \det(\mathbf{W}_k) \tag{29}$$

## B. Optimal Geometry of Special Cases

From Eq. (27), the value of  $\det(\mathbf{W}_k)$  is determined by the relative geometry of the target position vectors projected in the UAV body frame. Leveraging the geometrical interpretation of  $\det(\mathbf{W}_k)$ , several propositions can be given to provide better insights into the relative geometry optimization problem. In the following propositions, we use  $\gamma_{ij} \in [0, \pi]$  to denote the angle between vectors  $\mathbf{P}_{b,i}$  and  $\mathbf{P}_{b,j}$ , i.e., the two target position vectors in the UAV body frame.

**Proposition 2.** *If  $k = 2$  and the distances between the UAV and the cooperative target at time instant  $t_1$  and  $t_2$ , i.e.,  $\rho_1$  and  $\rho_2$ , are given, the optimal UAV-target geometry is given*

$$\det(\mathbf{W}_k) = \begin{cases} \sum_{i=1}^k \rho_i^2 \|\mathbf{P}_{b,1} \times \mathbf{P}_{b,2}\|^2, & k = 2 \\ \sum_{i=1}^k \rho_i^2 \sum_{1 \leq i < j \leq k} \|\mathbf{P}_{b,i} \times \mathbf{P}_{b,j}\|^2 - \sum_{1 \leq i < j < m \leq k} [(\mathbf{P}_{b,i} \times \mathbf{P}_{b,j}) \cdot \mathbf{P}_{b,m}]^2, & k \geq 3 \end{cases} \quad (27)$$

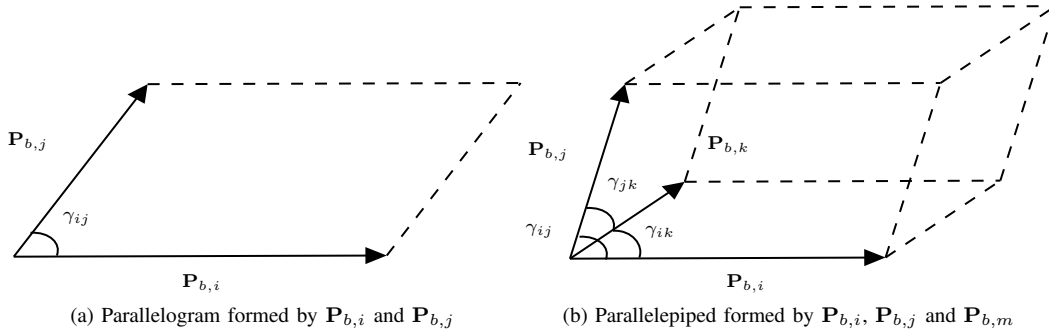


Fig. 2. Geometric interpretations on the terms of observability Gramian.

by

$$\gamma_{12} = \frac{\pi}{2} \quad (30)$$

*Proof.* Based on the definition of cross-product, the determinant of  $\mathbf{W}_k$  with  $k = 2$  can be rewritten as

$$\det(\mathbf{W}_2) = (\rho_1^2 + \rho_2^2) \rho_1^2 \rho_2^2 \sin^2 \gamma_{12} \quad (31)$$

It is clear that if the values of  $\rho_1$  and  $\rho_2$  are fixed, the maximum value of  $\det(\mathbf{W}_2)$  is achieved when  $\gamma_{12} = \frac{\pi}{2}$ . The corresponding configuration is depicted in Fig. 3, where the hollow circle stands for the origin of UAV body frame, and the black circles for the positions of the cooperative target in the UAV body frame.  $\square$

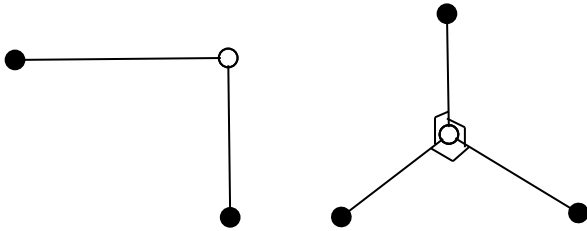


Fig. 3. Optimal configuration when  $k = 2$ . Fig. 4. Optimal configuration when  $k = 3$ .

**Proposition 3.** *If there are three sets of observations, i.e.,  $k = 3$ , and the distance between the UAV and the cooperative target is a constant, i.e.,  $\rho_1 = \rho_2 = \rho_3 = \rho$ , the optimal UAV-target configuration should satisfy the following condition (see Fig. 4)*

$$\gamma_{12} = \frac{\pi}{2}, \gamma_{13} = \frac{\pi}{2}, \gamma_{23} = \frac{\pi}{2} \quad (32)$$

*Proof.* According to [36], the volume of the parallelepiped constructed by vectors  $\mathbf{P}_{b,i}$ ,  $\mathbf{P}_{b,j}$  and  $\mathbf{P}_{b,m}$  can be expressed by the length of the vectors and three angles between them as

$$\text{vol}(\mathcal{P}(\mathbf{P}_{b,i}, \mathbf{P}_{b,j}, \mathbf{P}_{b,m})) = \|\mathbf{P}_{b,i}\| \|\mathbf{P}_{b,j}\| \|\mathbf{P}_{b,m}\| \sqrt{1 + 2 \cos \gamma_{ij} \cos \gamma_{im} \cos \gamma_{jm} - \cos^2 \gamma_{ij} - \cos^2 \gamma_{im} - \cos^2 \gamma_{jm}} \quad (33)$$

Substituting Eq. (33) and the formula for the area of a parallelogram into Eq. (27) in case of  $k = 3$ , we have

$$\begin{aligned} \det(\mathbf{W}_3) &= (\rho_1^2 + \rho_2^2 + \rho_3^2)(\rho_1^2 \rho_2^2 \sin^2 \gamma_{12} + \rho_1^2 \rho_3^2 \sin^2 \gamma_{13} + \rho_2^2 \rho_3^2 \sin^2 \gamma_{23}) \\ &\quad - \rho_1^2 \rho_2^2 \rho_3^2 (1 - \cos^2 \gamma_{12} - \cos^2 \gamma_{13} - \cos^2 \gamma_{23} + 2 \cos \gamma_{12} \cos \gamma_{13} \cos \gamma_{23}) \\ &= \rho_1^2 \rho_2^2 (\rho_1^2 + \rho_2^2) \sin^2 \gamma_{12} + \rho_1^2 \rho_3^2 (\rho_1^2 + \rho_3^2) \sin^2 \gamma_{13} + \rho_2^2 \rho_3^2 (\rho_2^2 + \rho_3^2) \sin^2 \gamma_{23} \\ &\quad - 2 \rho_1^2 \rho_2^2 \rho_3^2 \cos \gamma_{12} \cos \gamma_{13} \cos \gamma_{23} + 2 \rho_1^2 \rho_2^2 \rho_3^2 \end{aligned} \quad (34)$$

When  $\rho_1 = \rho_2 = \rho_3 = \rho$ , Eq. (34) can be reduced to

$$\det(\mathbf{W}_3) = 2\rho^6 (\sin^2 \gamma_{12} + \sin^2 \gamma_{13} + \sin^2 \gamma_{23} - \cos \gamma_{12} \cos \gamma_{13} \cos \gamma_{23} + 1) \quad (35)$$

Denote  $J$  as a function of the three relative angles as

$$J = \sin^2 \gamma_{12} + \sin^2 \gamma_{13} + \sin^2 \gamma_{23} - \cos \gamma_{12} \cos \gamma_{13} \cos \gamma_{23} + 1 \quad (36)$$

Since the distance  $\rho$  is a constant, maximizing the value of  $J$  yields the same result as optimizing  $\det(\mathbf{W}_3)$ . Note that the value of the angles between three vectors are constrained by each other. Taking  $\gamma_{23}$  as an example, its range can be easily determined by geometric relationship when  $\gamma_{12}$  and  $\gamma_{13}$  are given. As is depicted in Fig. 5, the extreme value of  $\gamma_{23}$  is reached when the three vectors are coplanar. The minimum value is obtained when vectors  $\mathbf{V}_2$  and  $\mathbf{V}_3$  are on the same side of  $\mathbf{V}_1$ , while the maximum is achieved when  $\mathbf{V}_2$  and  $\mathbf{V}_3$

are placed on the different side. If the values of  $\gamma_{12}$  and  $\gamma_{13}$  are both smaller than  $\frac{\pi}{2}$  (see Fig. 5 (a)), the range of  $\gamma_{23}$  is given by

$$|\gamma_{12} - \gamma_{13}| < \gamma_{23} < |\gamma_{12} + \gamma_{13}| \quad (37)$$

If one of the values of  $\gamma_{12}$  and  $\gamma_{13}$  is smaller than  $\frac{\pi}{2}$ , and the other one is larger than  $\frac{\pi}{2}$ , the range of  $\gamma_{23}$  is

$$|\gamma_{12} - \gamma_{13}| \leq \gamma_{23} \leq \min(|\gamma_{12} + \gamma_{13}|, 2\pi - |\gamma_{12} + \gamma_{13}|) \quad (38)$$

For the case of Fig. 5 (c), i.e., both  $\gamma_{12}$  and  $\gamma_{13}$  are larger than  $\frac{\pi}{2}$ ,  $\gamma_{23}$  is constrained by

$$|\gamma_{12} - \gamma_{13}| < \gamma_{23} < 2\pi - |\gamma_{12} + \gamma_{13}| \quad (39)$$

Taking the three angles  $\gamma_{12}$ ,  $\gamma_{13}$  and  $\gamma_{23}$  as the optimization variables, i.e.,

$$\Gamma = [\gamma_{12}, \gamma_{13}, \gamma_{23}]^T \quad (40)$$

and combining Eqs. (37)-(39), the configuration optimization problem with three observations is formulated as

$$\max_{\Gamma} J \quad (41)$$

subject to

$$|\gamma_{12} - \gamma_{13}| \leq \gamma_{23} \leq \min(\gamma_{12} + \gamma_{13}, 2\pi - (\gamma_{12} + \gamma_{13})) \quad (42)$$

Since it is difficult to solve the above optimization problem analytically, numerical search method is employed to find the solution. In Fig. 6, the value of  $J$  is depicted as a function of  $\gamma_{12}$ ,  $\gamma_{13}$  and  $\gamma_{23}$ , and the slices are taken at  $\gamma_{12} = \frac{\pi}{4}, \frac{\pi}{2}, \frac{3\pi}{4}$ ,  $\gamma_{13} = \frac{\pi}{2}$  and  $\gamma_{23} = \frac{\pi}{2}$  to visualize the change of  $J$ . The feasible region of the optimization problem, described by Eq. (42), turns out to be a regular tetrahedron as demonstrated in Fig. 7. From Figs. 6 and 7, it can be observed that  $\det(\mathbf{W}_3)$  equals to zero at the vertices of the feasible region, which corresponds to the cases that the three relative position vectors are collinear. This is consistent with Proposition 1 drawn from the geometrical interpretation. In Fig. 6, one can also note that the points in the central region yields larger value of the objective function compared to those in the marginal region. Since the central area of the definition domain, where the maximum value of  $J$  is achieved, satisfies the constraints in Eq. (42), the solution to the three-scan configuration optimization problem is the same as that of the unconstrained problem (41). It is clear from Fig. 6 that the maximum value is attained at the point  $(\frac{\pi}{2}, \frac{\pi}{2}, \frac{\pi}{2})$ . The corresponding contour plot at  $\gamma_{12} = \frac{\pi}{2}$ ,  $\gamma_{13} = \frac{\pi}{2}$  and  $\gamma_{23} = \frac{\pi}{2}$  are given in Fig. 8, and the area inside the black rectangle represents the feasible region. Therefore, the optimal configuration with three observations satisfies

$$\gamma_{12} = \frac{\pi}{2}, \gamma_{13} = \frac{\pi}{2}, \gamma_{23} = \frac{\pi}{2} \quad (43)$$

which corresponds to the geometry depicted in Fig. 4.  $\square$

When the number of observations is larger than 3, i.e.,  $k \geq 4$ , and  $\rho_1 = \rho_2 = \dots = \rho_k = \rho$ , the optimization results of UAV-target configurations through exhaustive numerical search are given directly in Fig. 9, where the origin of the UAV body frame is at  $(0, 0, 0)$  and the unit vectors represent the relative target positions. The results reveal that there are three

kinds of configurations that yield the largest value of  $\det(\mathbf{W}_4)$ . The corresponding angles between the four relative position vectors are summarized in Table I. It can be noted from the relative angles in Table I that Configuration (1) puts the four target positions at the vertices of a regular tetrahedron centered on the UAV. Comparing to Configuration (1), Configuration (2) flips one of the relative target positions around the UAV, which results in the same value of the area-related and volume-related terms in  $\det(\mathbf{W}_k)$ . The third configuration describes a rectangular pyramid whose upper vertex locates at the UAV and the separation angles of the vectors share the same value as Configurations (1) and (2).

TABLE I  
OPTIMAL GEOMETRY FOR  $k = 4$

Configuration	Relative Angles
(1)	109.5°, 109.5°, 109.5°, 109.5°, 109.5°, 109.5°
(2)	70.5°, 70.5°, 70.5°, 109.5°, 109.5°, 109.5°
(3)	70.5°, 70.5°, 70.5°, 70.5°, 109.5°, 109.5°

In case of  $k = 5$ , there are several different configurations that yield the maximum value of  $\det(\mathbf{W}_5)$ , thus only typical ones are depicted in Fig. 10 to provide some insight about the problem.

The optimal configurations with small value of  $k$  suggest that the UAV tends to enforce the cooperative target distribute around it in the body frame as dispersive as possible. For offline boresight calibration, the above optimization results can be utilized to determine the relative geometry between the UAV and the cooperative target during data collection process. However, adjusting the measurement positions and attitudes of the UAV offline with human efforts is time-consuming. In practical applications, the gimballed camera and UAV platform are usually packaged separately during transportation for safety, and thus the calibration process is required to be conducted efficiently during the flight before the target localization task is triggered. For this reason, the next section develops a configuration optimization method considering the vehicle dynamics for automatic camera-IMU calibration.

## V. CONFIGURATION OPTIMIZATION FOR BORESIGHT CALIBRATION WITH VEHICLE MOTION CONSTRAINTS

In order to obtain the boresight calibration angles accurately and efficiently during a flight, this section proposes a configuration optimization algorithm considering the UAV motion constraints. The dynamic model of a quadrotor is introduced first to facilitate the development of the optimization algorithm.

### A. UAV Dynamics Model

The dynamics of a quadrotor is formulated as

$$\begin{aligned} \dot{\mathbf{P}}^u &= \mathbf{V} \\ \dot{\mathbf{V}} &= \mathbf{a} \\ \mathbf{a} &= (C_n^b)^T \frac{\mathbf{F}}{m} + \mathbf{G} \end{aligned} \quad (44)$$

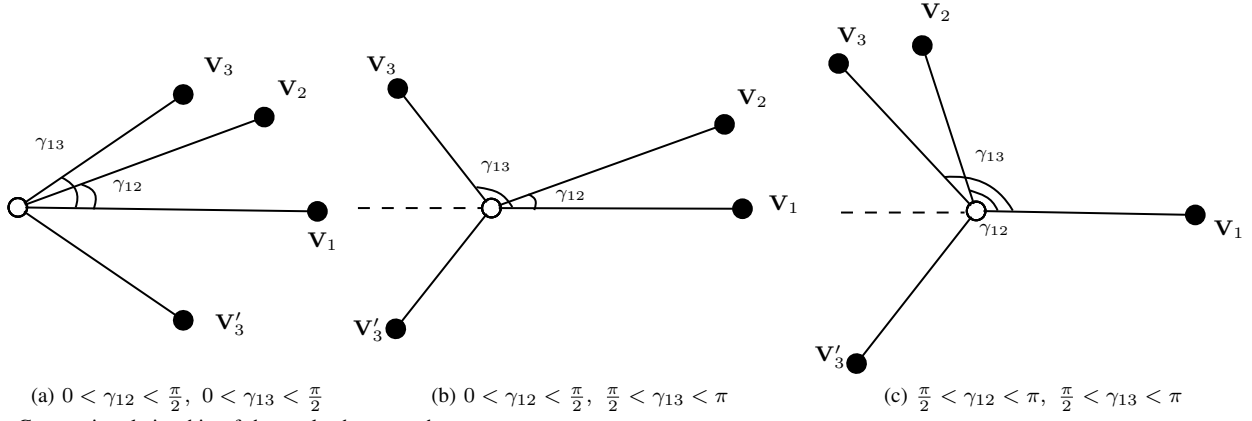


Fig. 5. Geometric relationship of the angles between three vectors.

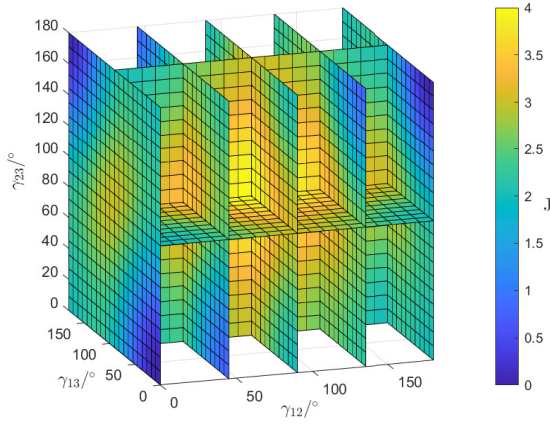


Fig. 6. The value of  $J$  as a function of  $\gamma_{12}$ ,  $\gamma_{13}$  and  $\gamma_{23}$ .

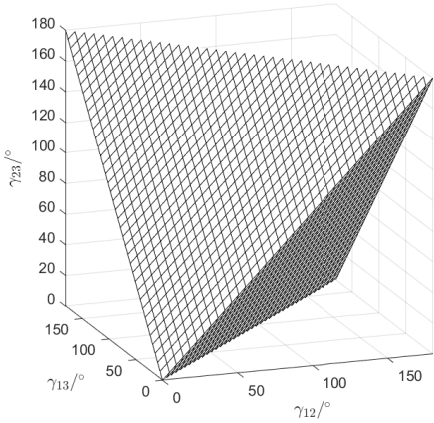


Fig. 7. Feasible region of the constrained optimization problem.

where  $\mathbf{V}$  and  $\mathbf{a} = [a^x, a^y, a^z]^T$  denote the velocity and acceleration of the UAV in the inertial frame, respectively. The vector  $\mathbf{G} = [0, 0, g]^T$  is the acceleration of gravity with  $g \approx 9.81m/s^2$  and  $m$  is the mass of the UAV. The symbol  $\mathbf{F} = [0, 0, -F_T]^T$  represents the thrust provided by rotors in the UAV body frame with  $F_T$  being the magnitude of the

thrust.

In this paper, the UAV is assumed to move at a constant altitude. Therefore, the vertical acceleration of the UAV equals zero, i.e.,  $a^z = 0$ . Accordingly, the horizontal accelerations can be expressed by the attitude angles as

$$\begin{aligned} a^x &= -g \frac{\sin(\phi) \sin(\psi) + \cos(\phi) \cos(\psi) \sin(\theta)}{\cos(\phi) \cos(\theta)} \\ a^y &= -g \frac{\cos(\phi) \sin(\psi) \sin(\theta) - \cos(\psi) \sin(\phi)}{\cos(\phi) \cos(\theta)} \end{aligned} \quad (45)$$

### B. Configuration Optimization During Flight

As derived in Sec. III, the observability of the boresight calibration system is determined by the target position in the body frame, i.e.,  $[x_b, y_b, z_b]^T$ . Thus both the position and attitude of the UAV can affect the system observability. According to Eqs. (44) and (45), the UAV position is obtained by the double integration of the inertial acceleration, which is determined by the attitude angles. Hence, the attitude at time  $t_k$  will affect the UAV position at time  $t_{k+2}$ , which further influences the degree of observability at time  $t_{k+2}$ . Therefore, a multi-step look-ahead optimization problem is constructed to avoid myopic performance in the UAV motion planning. Let  $T_p$  be the length of planning horizon and given the current attitude information, we take the attitude angles of the UAV from time  $t_{k+1}$  to  $t_{k+T_p}$  as the optimization variables, i.e.,

$$\begin{aligned} \Theta_k &= [\phi_{k+1}, \theta_{k+1}, \psi_{k+1}, \\ &\quad \phi_{k+2}, \theta_{k+2}, \psi_{k+2}, \dots, \phi_{k+T_p}, \theta_{k+T_p}, \psi_{k+T_p}]^T \end{aligned} \quad (46)$$

and the determinant of the observability Gramian at  $t_{k+T_p}$  is employed as the objective function at time  $t_k$ , i.e.,

$$J_k = \det(\mathbf{W}_{k+T_p}) \quad (47)$$

Considering the physical limits of the UAV, the configuration optimization problem at time  $t_k$  can be formulated as

$$\Theta_k^* = \arg \max_{\Theta_k} \{J_k\} \quad (48)$$

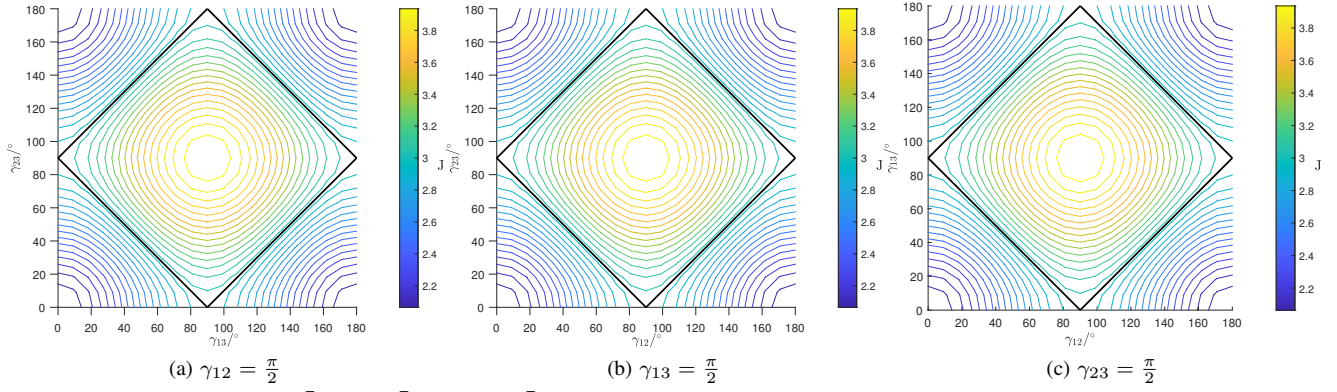


Fig. 8. Contour plot of  $J$  at  $\gamma_{12} = \frac{\pi}{2}$ ,  $\gamma_{13} = \frac{\pi}{2}$  and  $\gamma_{23} = \frac{\pi}{2}$ .

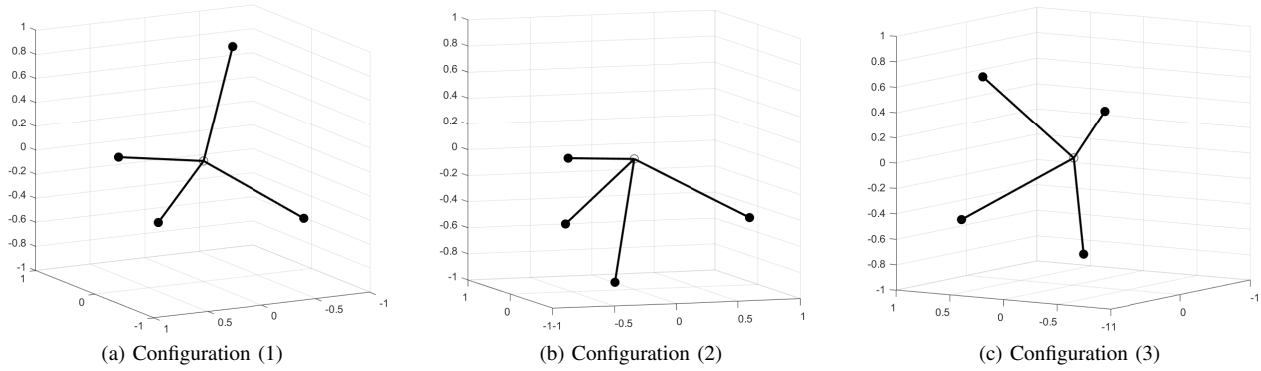


Fig. 9. Optimal UAV-target configurations for  $k = 4$ .

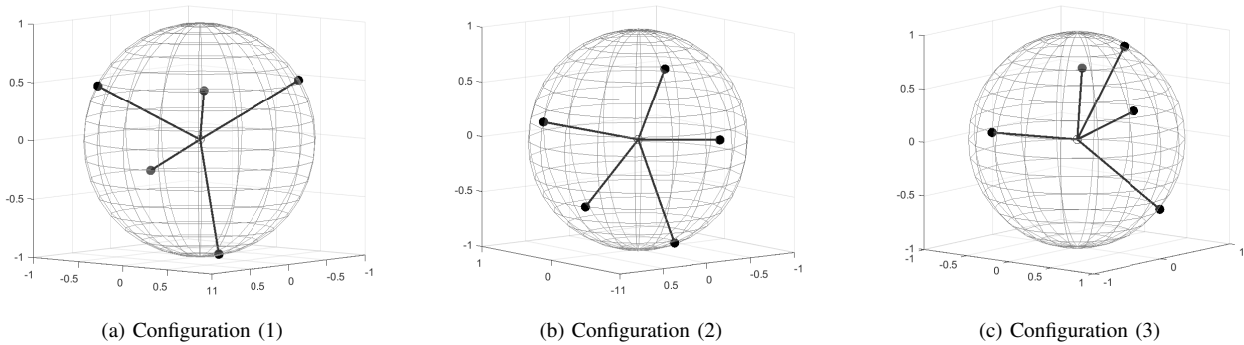


Fig. 10. Typical optimal UAV-target configurations for  $k = 5$ .

subject to

$$\begin{cases} |\dot{\phi}_l| \leq \dot{\phi}_{\max}, & |\phi_{l+1}| \leq \phi_{\max} \\ |\dot{\theta}_l| \leq \dot{\theta}_{\max}, & |\theta_{l+1}| \leq \theta_{\max} \\ |\dot{\psi}_l| \leq \dot{\psi}_{\max} \end{cases}, \quad l = k, \dots, k + T_p - 1 \quad (49)$$

where  $\dot{\phi}_l$ ,  $\dot{\theta}_l$  and  $\dot{\psi}_l$  are the angular rates of the attitude, and the subscript max denotes the maximum allowable turn rates and attitude angles of the UAV. Due to the physical limit of a quadrotor, the yaw rate is constrained by the maximum torque produced around the  $z$  axis of the body frame.

Because solving the above constrained optimization problem involves finding a time history of attitude angles that maximizes  $J_k$ , which is a highly nonlinear function, it is unlikely

to find an analytical solution to it. In this paper, we solve the multi-step optimization problem using CasADi toolbox [37], which finds the solution of a nonlinear programming problem (NLP) using the Interior-Point Method (IPM). The optimization is conducted every  $T_s$  seconds, and the trajectory planning is implemented in a receding-horizon manner. After each optimization process, the first set of attitude angles in the solution, i.e.,  $[\phi_{k+1}^*, \theta_{k+1}^*, \psi_{k+1}^*]^T$ , is applied to the control system to guide the UAV.

*Remark 1.* IPM is a Newton iteration-based method, and its computational complexity is related to the dimension of optimization vector and also the termination condition. The IPM algorithm yields an  $\varepsilon$ -complementary solution in at most

$\mathcal{O}(\sqrt{n} \log(1/\varepsilon))$  iterations, where  $n$  represents the number of optimization variables and  $\varepsilon$  is the tolerance on dual infeasibility [38]. The objective function in this paper is nonlinear, and thus the computation of Hessian matrix is required in each iteration. However, the objective function is in the form of a determinant and it is difficult to derive the computational complexity of this step. Therefore, we assume that in each iteration, the quasi-Newton method is used to update the optimization variable and the computational complexity is  $\mathcal{O}(n^2)$  [39]. Then the total computational complexity is approximated by  $\mathcal{O}(\sqrt{n} \log(1/\varepsilon)) \times \mathcal{O}(n) = \mathcal{O}(n^{\frac{3}{2}} \log(1/\varepsilon))$ , which reveals that the proposed optimization problem can be solved in a polynomial time. To investigate the practical computational complexity of the proposed algorithm, we have also tested its time cost under different conditions in the following section.

## VI. NUMERICAL STUDIES AND EXPERIMENTAL RESULTS

In this section, we show the simulation results of the observability-based trajectory optimization method for camera-IMU boresight calibration. The misalignment angles are estimated through linear regression and the estimation results are compared to that of the non-optimized trajectories. We also evaluate the computational complexity and present the experimental results of an in-door flight to validate the proposed trajectory optimization method.

### A. Simulation Setup

The simulation considers a UAV follows the optimized trajectory and collects information of a cooperative target for camera-IMU boresight calibration. The cooperative target is stationary and locates at (0m, 0m, 0m). The initial position of the UAV in the inertial frame is (-20m, 20m, 20m) and the attitude angles are initialized as (0°, 0°, 0°). The maximum allowable roll and pitch angle of the UAV are set to be  $\phi_{\max} = \pi/6$  rad and  $\theta_{\max} = \pi/6$  rad. The angular rates of attitude angles are constrained by  $\dot{\phi}_{\max} = \pi/4$  rad/s,  $\dot{\theta}_{\max} = \pi/4$  rad/s and  $\dot{\psi}_{\max} = \pi/4$  rad/s, respectively. Since the installation error in the  $z$  direction is generally larger than the other two angles, the ground truth of the misalignment angles are set as  $e_x = 5^\circ$ ,  $e_y = 5^\circ$ , and  $e_z = 10^\circ$ . The trajectory optimization process is carried out every 0.05s.

To illustrate the performance of the proposed configuration optimization method, the misalignment angles are estimated using the linear regression method. As stated in Sec. III, the parameter to be estimated is given by  $\mathbf{x} = [e_x, e_y, e_z]^T$ . Denote two set of measurement variables as

$$\mathbf{m}_1 = [\mathbf{P}^u, \mathbf{P}^t, \phi, \theta, \psi]^T, \quad \mathbf{m}_2 = [\mathbf{P}^u, \mathbf{P}^t, \alpha, \beta, u, v]^T \quad (50)$$

and the actual measurements from the onboard sensors are given by

$$\begin{aligned} \mathbf{z}_1 &= \mathbf{m}_1 + \mathbf{v}_1, & \mathbf{v}_1 &\sim (0, \mathbf{R}_1) \\ \mathbf{z}_2 &= \mathbf{m}_2 + \mathbf{v}_2, & \mathbf{v}_2 &\sim (0, \mathbf{R}_2) \end{aligned} \quad (51)$$

where  $\mathbf{v}_1$  and  $\mathbf{v}_2$  are Gaussian measurement noise with covariances  $\mathbf{R}_1$  and  $\mathbf{R}_2$  respectively.

We assume that  $\mathbf{R}_1$  and  $\mathbf{R}_2$  are diagonal matrices and thus can be expressed as

$$\begin{aligned} \mathbf{R}_1 &= \begin{bmatrix} \sigma_p^2 \mathbf{I}_3 & 0 & 0 \\ 0 & \sigma_p^2 \mathbf{I}_3 & 0 \\ 0 & 0 & \sigma_{att}^2 \mathbf{I}_3 \end{bmatrix}, \\ \mathbf{R}_2 &= \begin{bmatrix} \sigma_p^2 \mathbf{I}_3 & 0 & 0 & 0 \\ 0 & \sigma_p^2 \mathbf{I}_3 & 0 & 0 \\ 0 & 0 & \sigma_{los}^2 \mathbf{I}_2 & 0 \\ 0 & 0 & 0 & \sigma_{pix}^2 \mathbf{I}_2 \end{bmatrix} \end{aligned} \quad (52)$$

where  $\sigma_p = 0.3\text{m}$  and  $\sigma_{att} = 2^\circ$  are the measurement-error standard deviations of the position and attitude angles, while  $\sigma_{los} = 0.5^\circ$  and  $\sigma_{pix} = 3\text{px}$  are that of the gimbal angles and pixel coordinates of the cooperative target.

Suppose the number of scans is  $k$ , the minimum variance parameter estimate, as derived in Appendix A, is given by

$$\begin{aligned} \hat{\mathbf{x}} &= \left[ \sum_{i=1}^k \mathbf{H}_i (\mathbf{A}_i \mathbf{R}_1 \mathbf{A}_i^T + \mathbf{B}_i \mathbf{R}_2 \mathbf{B}_i^T)^{-1} \mathbf{H}_i^T \right]^{-1} \\ &\quad \times \sum_{i=1}^k \mathbf{H}_i (\mathbf{A}_i \mathbf{R}_1 \mathbf{A}_i^T + \mathbf{B}_i \mathbf{R}_2 \mathbf{B}_i^T)^{-1} (f_g(\mathbf{z}_{2i}) - f_b(\mathbf{z}_{1i})) \end{aligned} \quad (53)$$

where  $f_b$  and  $f_g$  are functions specified by the RHS of Eqs. (1) and (4), respectively.  $\mathbf{A}_i$  and  $\mathbf{B}_i$  denote the following partial derivatives

$$\mathbf{A}_i = \frac{\partial f_b}{\partial \mathbf{m}_1} \Big|_{\mathbf{z}_{1i}}, \quad \mathbf{B}_i = \frac{\partial f_g}{\partial \mathbf{m}_2} \Big|_{\mathbf{z}_{2i}} \quad (54)$$

### B. Characteristics of Proposed Trajectory Optimization

This subsection presents the simulation results and investigates the characteristics of the proposed observability-enhancement trajectory optimization approach. Since the proposed planning method is developed based on the concept of receding-horizon optimization, the length of the prediction horizon, i.e.,  $T_p$ , plays an important role in the planning performance. Comparison simulations with  $T_p = 4, 6, 8$  are conducted to investigate the influence of the horizon length. The trajectory optimization results of online boresight calibration is presented in Fig. 11, where the first row corresponds to the UAV trajectories in the inertial frame. It can be observed that the trajectory becomes smoother with larger value of  $T_p$ . The corresponding time histories of attitude angles are shown in Fig. 12. In Fig. 12, the magnitudes of attitude angles are smaller when the horizon length becomes larger. These two observations reveal that the myopic problem can be alleviated with longer planning horizon, which is the typical characteristic of the receding-horizon based method.

Since the objective function, i.e., the determinant of the observability Gramian, is determined by the target position vectors in the UAV body frame, the relative trajectories of the cooperative target are depicted in the second row of Fig. 11. The UAV locates at the origin of its body frame and relative positions of the target are calculated using Eq. (1). The determinant of observability Gramian matrices with different value of  $T_p$  are provided in Fig. 13 for comparison.

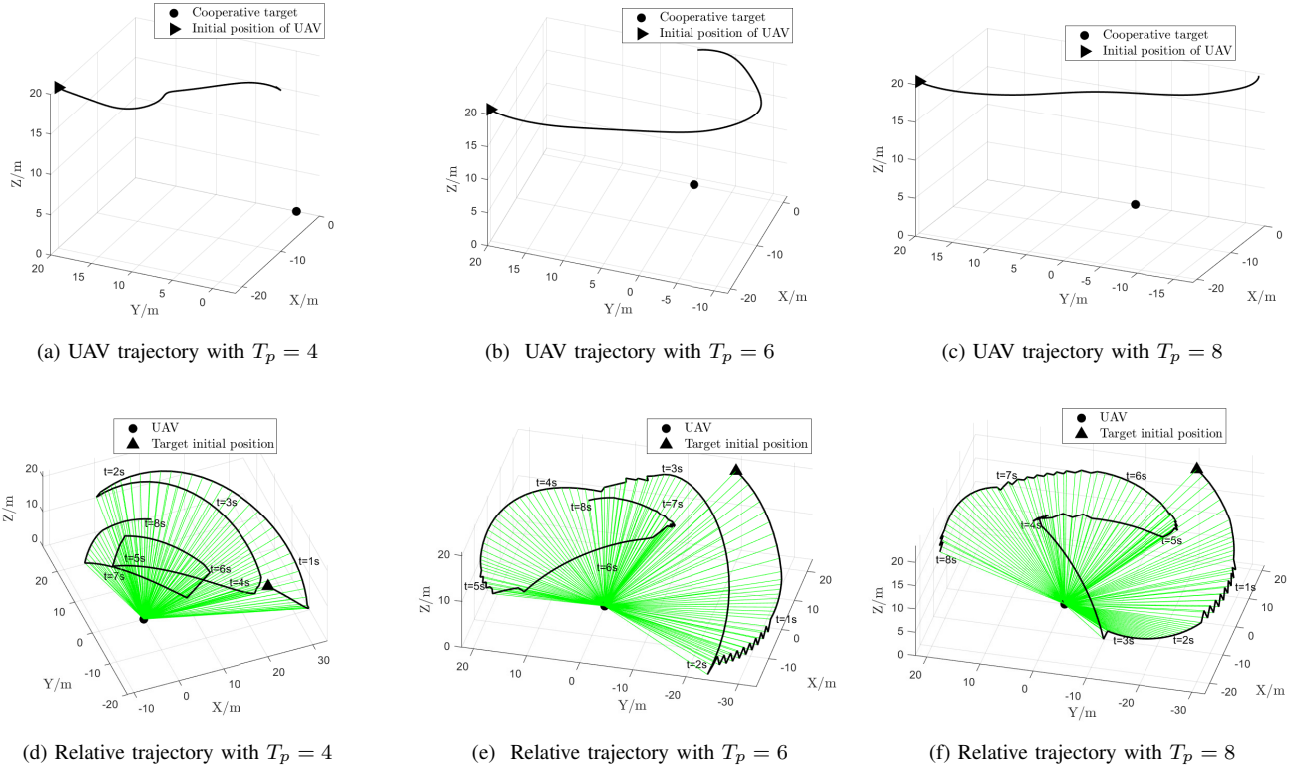


Fig. 11. Comparison of optimized trajectories with  $T_p = 4, 6, 8$ .

Recall the geometrical interpretation of Eq. (27),  $\det(\mathbf{W}_k)$  is governed by the parallelogram area and parallelepiped volume. From Fig. 11 (d)-(f), it can be noted that before time instant  $t = 3.8s$ , the average angle between the two main hook faces constructed by the relative position vectors with  $T_p = 4$  is smaller than that with  $T_p = 6$  and  $T_p = 8$ . As a result, the terms related to area and volume of geometries in Fig. 11 (d) are smaller compared to the others. However, the corresponding determinant of  $\mathbf{W}_k$  in Fig. 13 reaches higher value with  $T_p = 4$ , which implies that the volume-related terms dominate the objective function of the optimization problem before  $t = 3.8s$ . With the increase of the number of sampling times, the coefficient of the area-related terms in Eq. (27), i.e.,  $\sum_{i=1}^k \rho_i^2$ , also increases. Thus, the value of the determinant mainly depends on the summation of parallelogram area. Consequently, the value of  $\det(\mathbf{W}_k)$  with  $T_p = 4$  is overtaken by that with longer planning horizons, as shown in Fig. 13. For the same reason, the resulting value of the determinant with horizon length  $T_p = 8$  exceeds that with  $T_p = 6$  from time instant  $t = 6.3s$  at the price of lower value in the initial phase.

To validate the effectiveness of the proposed trajectory optimization method for boresight calibration, Monte-Carlo simulations are carried out to assess the performance of misalignment angle estimation. In each Monte-Carlo experiment, the start point of the UAV is randomly sampled from a cuboid area, i.e.,  $x \in [-30m, 30m]$ ,  $y \in [-30m, 30m]$ ,  $z \in [20m, 50m]$ . The simulation time of each run is set as 8s. It is assumed that the UAV is in the hovering mode at the beginning of the calibration process, i.e., the roll and pitch

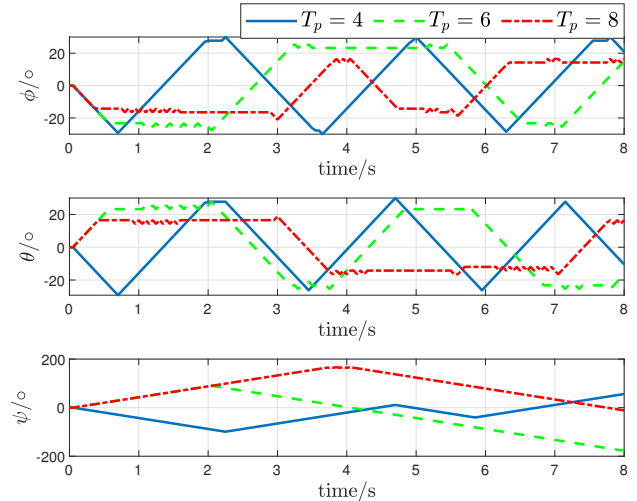


Fig. 12. Time histories of UAV attitude angles.

angle are both set to be  $0^\circ$  initially. The initial value of the yaw angle is randomly selected from  $[-\pi, \pi]$  at each run. The mean and standard deviation of misalignment angle estimation error from 100 Monte-Carlo runs with different value of  $T_p$  are summarized in Table II. From this table, it can be noted that the mean of estimation errors are all lower than  $0.5^\circ$ . This means that the target localization accuracy will be significantly enhanced through boresight misalignment calibration. One can also observe that the estimation performance can be improved by increasing the value of  $T_p$ , which is consistent with the simulation results of  $\det(\mathbf{W}_k)$  in Fig. 13.

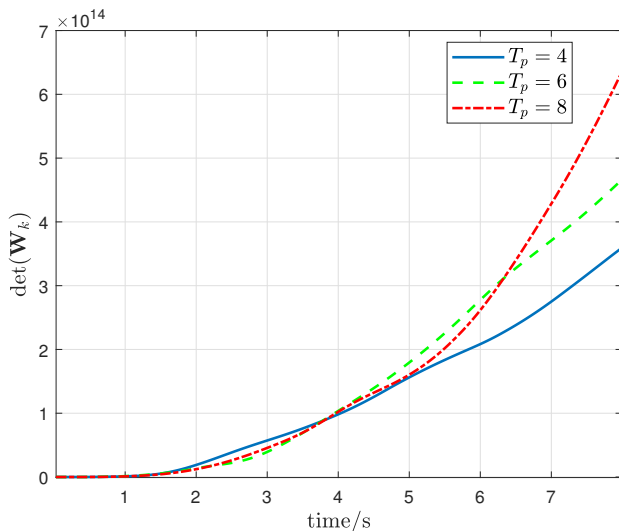


Fig. 13. Determinant of observability Gramian.

TABLE II  
ESTIMATION ERROR FROM MONTE-CARLO SIMULATIONS

		Estimation error of $e_x$ (deg)	Estimation error of $e_y$ (deg)	Estimation error of $e_z$ (deg)
$T_P = 4$	Mean	0.4409	0.3854	0.4377
	Std	0.4764	0.4340	0.5116
$T_P = 6$	Mean	0.3703	0.3400	0.4019
	Std	0.2549	0.4203	0.3785
$T_P = 8$	Mean	0.3049	0.3287	0.3431
	Std	0.2702	0.3572	0.3951

*Remark 2.* Since the UAV is assumed to fly at a constant altitude and the roll, pitch angles are constrained by the physical limits, the variation of the  $z$  coordinate of the target in the body frame, i.e.,  $z_{b,i}$ , is limited during the data collecting process. As a result, if the start point of the UAV is set with a low altitude, the value of  $z_{b,i}$  will remain small, compared to the horizontal coordinates  $x_{b,i}$  and  $y_{b,i}$ . According to Eqs. (15) and (16), the observability of the individual misalignment angle is influenced by the corresponding diagonal element of  $\mathbf{W}_k$ . Because the first two diagonal elements contains the term  $z_{b,i}^2$ , the estimation errors of  $e_x$  and  $e_y$  tend to be relatively large if the UAV starts to move at a low altitude. For this reason, we set the initial altitude of the UAV to be  $z \in [20m, 50m]$  in the Monte-Carlo simulations.

### C. Comparison with Non-optimized Trajectory

Notice that most existing sensor bias calibrations works assume that the bias is modeled as additive and multiplicative errors. However, the calibration of boresight misalignment involves estimating the rotational relationship between the IMU and camera frames. Hence, we compare the estimation results generated by the proposed optimized trajectory and the non-optimized trajectories to further demonstrate the advantage of the proposed method. Two typical scenarios are considered to generate the non-optimized trajectories: flyby and random maneuver. In flyby cases, the three attitude angles of the UAV are randomly generated initially and keep constant during the data collection process, thus the UAV moves along a straight

line in this mode. For the random maneuver scenarios, the attitude angles are randomly sampled from the corresponding permissible ranges at each time instant and the waypoints are integrated accordingly using the UAV dynamics. The optimized trajectories are generated using the proposed method with  $T_P = 6$ . Monte-Carlo experiments are implemented for 100 times in each scenario. The initial conditions of the UAV in Monte-Carlo runs are consistent with that of Sec. VI-B and the ground truth of the boresight misalignment angles are randomly selected from  $e_x \in [-5^\circ, 5^\circ]$ ,  $e_y \in [-5^\circ, 5^\circ]$  and  $e_z \in [-10^\circ, 10^\circ]$  in each trial. The comparison results in Fig. 14 shows the Mean Absolute Error (MAE) of misalignment angles with different UAV trajectories. The figure reveals that through attitude and trajectory optimization, the error of misalignment estimation converges faster and achieves a lower value compared to the non-optimized ones. The statistical descriptions of the final estimation error with the three different trajectories are summarized in Table III. It can be clearly observed from the table that the mean and standard deviation of misalignment angle estimation errors decrease through the observability-enhancement trajectory optimization. This reveals that higher accuracy of bearing-only target localization can be guaranteed by utilizing the proposed trajectory planing method for camera-IMU boresight calibration.

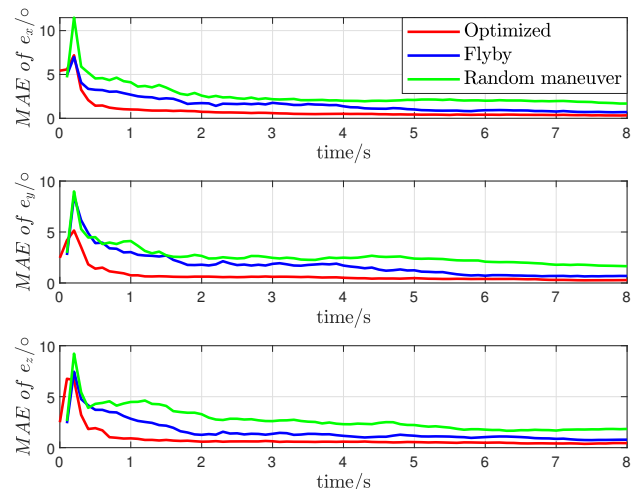


Fig. 14. Comparison of MAE with different trajectories.

TABLE III  
ESTIMATION RESULTS WITH DIFFERENT TRAJECTORIES

		Estimation error of $e_x$ (deg)	Estimation error of $e_y$ (deg)	Estimation error of $e_z$ (deg)
Optimized	Mean	0.3365	0.2848	0.4454
	Std	0.4193	0.3722	0.5116
Random maneuver	Mean	1.6821	1.6459	1.8352
	Std	1.8130	1.8566	1.1982
Flyby	Mean	0.7051	0.6865	0.7826
	Std	0.9015	0.8146	0.9261

### D. Computational Complexity Analysis

In our trajectory optimization problem, the dimension of optimization vector is determined by the prediction horizon

length, i.e.,  $n = 3T_P$ . Thus, we tested the mean execution time of the planning process with different prediction length. The initial position and attitude of the UAV are set to be  $[-30m, -30m, -40m]$  and  $[0^\circ, 0^\circ, 0^\circ]$ . The ground truth of the misalignment angles are  $[5^\circ, 5^\circ, 10^\circ]$  in all simulation runs for fair comparison. The trajectory optimization algorithm is conducted every  $0.2s$ . The default value of the maximum iteration times is set as 2000 and the termination tolerance is  $10^{-4}$ . The simulations are conducted in a personal computer environment with i5-8265U and 8 GB RAM. Figure 15 shows the mean execution time for  $T_P$ -step planning. From the figure, the planning process can be accomplished in  $0.12s$  when the prediction horizon is shorter than 14.

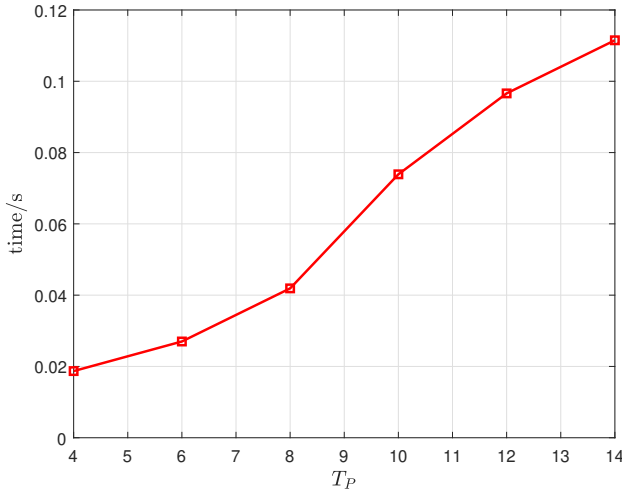


Fig. 15. The mean execution time with different  $T_P$ .

The boresight misalignment estimation error after applying the first sequence of attitude angles optimized from the proposed method with different value of  $T_P$  are summarized in Table. IV. Unsurprisingly, it can be observed from the table that the estimation error becomes smaller with larger prediction horizon length at the cost of more computational time. One can also note that with  $T_P = 12, 14$ , the estimation accuracy improves slightly compared to that with  $T_P = 10$ . The reason is that with longer planning horizon, the prediction of the UAV and target states may deviate further from the future truth, which results in the inaccuracy of the objective function and influences the optimality of the attitude angles at current time instant. Therefore, an appropriate value of  $T_P$  can be selected by balancing the computational cost and the estimation accuracy.

TABLE IV  
EXECUTION TIME AND ESTIMATION ERROR WITH DIFFERENT  $T_P$

	Estimation error (deg)			Execution time (s)
	$\Delta e_x$	$\Delta e_y$	$\Delta e_z$	
$T_P = 4$	13.9363	12.5252	18.9506	0.0156
$T_P = 6$	11.5715	10.9989	20.8501	0.0289
$T_P = 8$	8.8150	7.7356	11.3089	0.0426
$T_P = 10$	5.4036	4.6016	9.0729	0.0742
$T_P = 12$	5.8427	3.4935	7.6091	0.0971
$T_P = 14$	4.4725	4.4795	8.6643	0.1124

As mentioned before, the computational complexity of the

iteration-based optimization problem is also influenced by the predefined termination condition. Thus we have tested the execution time with different value of  $\epsilon$ . The prediction horizon length is set to be  $T_P = 6$  and the maximum iteration times is set as 3000 in the simulations. The mean execution time simulation results are presented in Fig. 16, and the time cost increases linearly with the logarithm of  $\epsilon$ . The estimation error after a single-step planning is given in Table. V. With lower termination tolerance, it spends more time for the optimization solver to achieve the desired termination condition. But the estimation errors after implementing the optimized actions with smaller  $\epsilon$  become smaller in general. Thus, one can impose a trade-off between the time cost and the performance of the estimator.

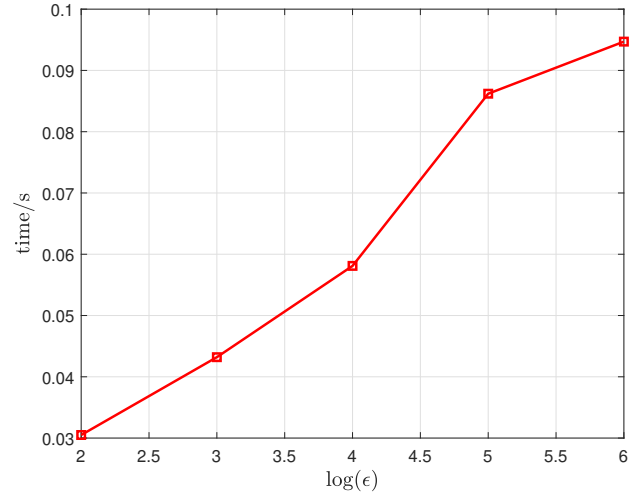


Fig. 16. The mean execution time with different  $\epsilon$ .

TABLE V  
EXECUTION TIME AND ESTIMATION ERROR WITH DIFFERENT  $\epsilon$

	Estimation error (deg)			Execution time (s)
	$\Delta e_x$	$\Delta e_y$	$\Delta e_z$	
$\epsilon = 10^{-2}$	9.0703	12.4950	12.8779	0.0314
$\epsilon = 10^{-3}$	9.2000	9.3306	7.1543	0.0452
$\epsilon = 10^{-4}$	8.8286	8.2802	11.2697	0.0592
$\epsilon = 10^{-5}$	6.3995	4.3377	6.5261	0.0866
$\epsilon = 10^{-6}$	4.2019	5.5338	4.7021	0.0951

### E. Experimental Results

The proposed trajectory optimization method is also experimentally evaluated indoor aided by the VICON motion capture system. As shown in Fig. 17, a gimbaled-camera is mounted on a floor stand, which simulates the UAV during the experiment. The attitudes and positions of the stand and the target can be acquired from the VICON system. The cooperative target locates at  $(2m, 3m, 0m)$  and the initial position of the camera is  $(-2m, 3m, 1.7m)$ . Optimized trajectory and the corresponding attitude of the UAV are generated using the proposed method with the length of planning horizon being  $T_P = 6s$ . A straight-line trajectory with a constant roll attitude angle  $\phi_0 = -5^\circ$  is used for performance comparison. The optimized and straight-line trajectories are shown in Fig. 18, where the

actual sampling data from the VICON system are also plotted. The estimation results of the boresight misalignment angles with different trajectories are given in Table VI.

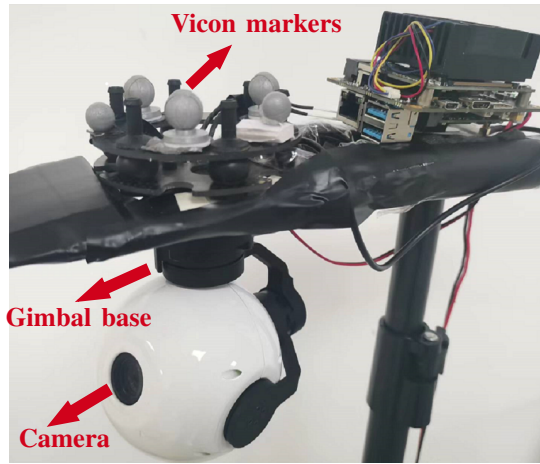


Fig. 17. Integrated camera and attitude sensor system.

TABLE VI  
ESTIMATION RESULTS OF MISALIGNMENT ANGLES WITH DIFFERENT TRAJECTORIES

	Estimation of $e_x$ (deg)	Estimation of $e_y$ (deg)	Estimation of $e_z$ (deg)
With optimization	3.8972	-2.1584	2.2612
Without optimization	2.5036	-0.1735	0.7746

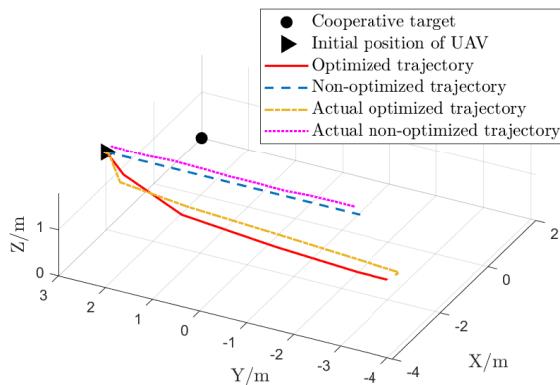


Fig. 18. Optimal UAV trajectory employed in the experiment.

The performance of the proposed trajectory optimization method is evaluated by an extra target localization process since the ground truth values of the boresight misalignment angles are not available. To ensure the observability of the bearing-only localization, the UAV follows a semi-circular trajectory centered on the target. The commonly-used extended Kalman filter (EKF) is employed as the estimator and the initial value of the states is obtained under a flat-ground assumption, which means the distance between the UAV and the target can be roughly calculated using the altitude of the UAV. The comparison results of the localization error are

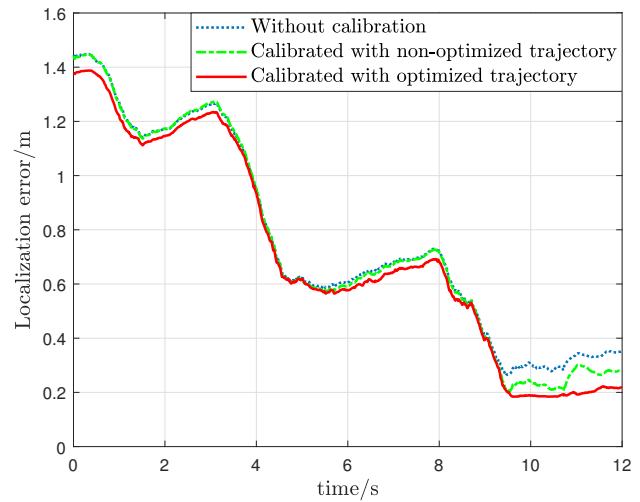


Fig. 19. Comparison results of target localization error.

shown in Fig. 19. The results show that the target localization performance can be improved by calibrating the misalignment errors between the IMU and camera gimbal. It can also be clearly observed that with the calibration result using optimized trajectory, the final localization error is reduced by nearly 25% compared to the non-optimized trajectory.

## VII. CONCLUSION

To improve the performance of boresight calibration for the integrated camera-IMU system using a cooperative target, this paper analyzes the observability of the misalignment angles based on observability Gramian. It is found that the degree of observability is determined by the geometrical configuration between the UAV and the target in the UAV body frame. A scalar measure of observability Gramian is selected as the optimization criterion and optimal configurations are obtained based on numerical approach. To autonomously calibrate the misalignment angles during a flight, we further develop an online two-dimensional trajectory optimization method considering the UAV dynamic constraint. Extensive numerical simulations and in-door flight experimental results show that by actively enhancing the system observability, the accuracy and efficiency of sensor boresight calibration process are both improved using the proposed approach. However, since the proposed trajectory optimization approach simultaneously determines the desired attitude and position of the UAV at next time instant, it cannot guarantee that the cooperative target keeps being detected due to the occlusion of fuselage and limited field of view (FOV) of the onboard camera. Therefore, extra constraints should be considered in the proposed trajectory design method according to the physical properties of the UAVs and sensors employed in practical use.

APPENDIX A  
DERIVATION OF EQ. (53)

Note that Eqs. (1) and (4) can be expressed as

$$\begin{bmatrix} x_b \\ y_b \\ z_b \end{bmatrix} = f_b(\mathbf{m}_1) = f_b(\mathbf{z}_1 - \mathbf{v}_1), \quad \begin{bmatrix} x_g \\ y_g \\ z_g \end{bmatrix} = f_g(\mathbf{m}_2) = f_g(\mathbf{z}_2 - \mathbf{v}_2) \quad (55)$$

Using Taylor expansion and ignoring the higher-order terms yields

$$\begin{bmatrix} x_b \\ y_b \\ z_b \end{bmatrix} = f_b(\mathbf{z}_1) - \frac{\partial f_b}{\partial \mathbf{m}_1} \Big|_{\mathbf{z}_1} \cdot \mathbf{v}_1, \quad \begin{bmatrix} x_g \\ y_g \\ z_g \end{bmatrix} = f_g(\mathbf{z}_2) - \frac{\partial f_g}{\partial \mathbf{m}_2} \Big|_{\mathbf{z}_2} \cdot \mathbf{v}_2 \quad (56)$$

Substituting Eq. (56) into Eq. (6), we have

$$f_g(\mathbf{z}_2) - f_b(\mathbf{z}_1) = \tilde{\mathbf{H}}\mathbf{x} - \frac{\partial f_b}{\partial \mathbf{m}_1} \Big|_{\mathbf{z}_1} \cdot \mathbf{v}_1 + \frac{\partial f_g}{\partial \mathbf{m}_2} \Big|_{\mathbf{z}_2} \cdot \mathbf{v}_2 \quad (57)$$

where  $\tilde{\mathbf{H}}$  is the Jacobian matrix

$$\tilde{\mathbf{H}} = \begin{bmatrix} 0 & -\tilde{z}_b & \tilde{y}_b \\ \tilde{z}_b & 0 & -\tilde{x}_b \\ -\tilde{y}_b & \tilde{x}_b & 0 \end{bmatrix} \quad (58)$$

with  $[\tilde{x}_b, \tilde{y}_b, \tilde{z}_b]^T$  denoting the noise-corrupted position vector calculated by  $f_b(\mathbf{z}_1)$ .

Suppose that  $k(\geq 2)$  scans of measurements are collected at discrete time instants  $i = 1, 2, \dots, k$ , a linear regression problem about  $\mathbf{x}$  can be established by stacking Eq. (57) as

$$\begin{bmatrix} f_g(\mathbf{z}_{2_1}) - f_b(\mathbf{z}_{1_1}) \\ \vdots \\ f_g(\mathbf{z}_{2_k}) - f_b(\mathbf{z}_{1_k}) \end{bmatrix} = \begin{bmatrix} \tilde{\mathbf{H}}_1 \\ \vdots \\ \tilde{\mathbf{H}}_k \end{bmatrix} \mathbf{x} + \mathbf{V} \quad (59)$$

where  $\mathbf{V}$  is a zero-mean noise with covariance

$$\mathbf{R} = \text{diag} \left( \left\{ \mathbf{A}_i \mathbf{R}_1 \mathbf{A}_i^T + \mathbf{B}_i \mathbf{R}_2 \mathbf{B}_i^T \right\}_{i=1}^k \right) \quad (60)$$

According to [40], the solution of Eq. (59) is given by Eq. (53).

Note that we truncate the higher-order terms in Taylor expansion when formulating the linear estimation problem in Eq. (59). As can be seen in Eqs. (57) and (59), ignoring the higher-order terms about sensor noise mainly influences the covariance of the residual error in the least squares problem, i.e.,  $\mathbf{R}$ , which is an adjustable parameter and can be tuned according to the quality of sensors in practical use. Thus the simplification is reasonable and helps to obtain an analytical solution of the misalignment angle estimation problem by using the weighted least squares (WLS) method, which is time-efficient and suitable for online applications.

REFERENCES

[1] J. Gu, T. Su, Q. Wang, X. Du, and M. Guizani, "Multiple moving targets surveillance based on a cooperative network for multi-uav," *IEEE Communications Magazine*, vol. 56, no. 4, pp. 82–89, 2018.

[2] V. Šmídl and R. Hofman, "Tracking of atmospheric release of pollution using unmanned aerial vehicles," *Atmospheric Environment*, vol. 67, pp. 425–436, 2013.

[3] T. Moranduzzo and F. Melgani, "Detecting cars in uav images with a catalog-based approach," *IEEE Transactions on Geoscience and Remote Sensing*, vol. 52, no. 10, pp. 6356–6367, 2014.

[4] T. Tomic, K. Schmid, P. Lutz, A. Domel, M. Kassecker, E. Mair, I. L. Grixia, F. Ruess, M. Suppa, and D. Burschka, "Toward a fully autonomous uav: Research platform for indoor and outdoor urban search and rescue," *IEEE robotics & automation magazine*, vol. 19, no. 3, pp. 46–56, 2012.

[5] S. He, H.-S. Shin, S. Xu, and A. Tsourdos, "Distributed estimation over a low-cost sensor network: A review of state-of-the-art," *Information Fusion*, vol. 54, pp. 21–43, 2020.

[6] S. He, H.-S. Shin, and A. Tsourdos, "Trajectory optimization for multitarget tracking using joint probabilistic data association filter," *Journal of Guidance, Control, and Dynamics*, vol. 43, no. 1, pp. 170–178, 2020.

[7] —, "Trajectory optimization for target localization with bearing-only measurement," *IEEE Transactions on Robotics*, vol. 35, no. 3, pp. 653–668, 2019.

[8] M. Pachter, N. Ceccarelli, and P. R. Chandler, "Vision-based target geolocation using micro air vehicles," *Journal of guidance, control, and dynamics*, vol. 31, no. 3, pp. 597–615, 2008.

[9] M. E. Campbell and M. Wheeler, "Vision-based geolocation tracking system for uninhabited aerial vehicles," *Journal of guidance, control, and dynamics*, vol. 33, no. 2, pp. 521–532, 2010.

[10] S. Sohn, B. Lee, J. Kim, and C. Kee, "Vision-based real-time target localization for single-antenna gps-guided uav," *IEEE Transactions on Aerospace and Electronic Systems*, vol. 44, no. 4, pp. 1391–1401, 2008.

[11] D. B. Barber, J. D. Redding, T. W. McLain, R. W. Beard, and C. N. Taylor, "Vision-based target geo-location using a fixed-wing miniature air vehicle," *Journal of Intelligent and Robotic Systems*, vol. 47, no. 4, pp. 361–382, 2006.

[12] X. Zhang, W. Xue, X. He, and H. Fang, "Distributed filter with biased measurements: A scalable bias-correction approach," *IEEE Transactions on Signal and Information Processing over Networks*, vol. 8, pp. 844–854, 2022.

[13] Y. Wang, J. Wang, S. He, H.-S. Shin, and A. Tsourdos, "Optimal guidance with active observability enhancement for scale factor error estimation of strapdown seeker," *IEEE Transactions on Aerospace and Electronic Systems*, vol. 57, no. 6, pp. 4347–4362, 2021.

[14] A. Tokta and A. K. Hocoaglu, "Sensor bias estimation for track-to-track association," *IEEE Signal Processing Letters*, vol. 26, no. 10, pp. 1426–1430, 2019.

[15] L. Zhang, F. Deng, J. Chen, Y. Bi, S. K. Phang, and X. Chen, "Trajectory planning for improving vision-based target geolocation performance using a quad-rotor uav," *IEEE Transactions on Aerospace and Electronic Systems*, vol. 55, no. 5, pp. 2382–2394, 2018.

[16] X. Yang, S. He, H.-S. Shin, and A. Tsourdos, "Trajectory optimization for target localization and sensor bias calibration with bearing-only information," *Guidance, Navigation and Control*, vol. 2, no. 03, p. 2250015, 2022.

[17] N. N. Okello and S. Challa, "Joint sensor registration and track-to-track fusion for distributed trackers," *IEEE Transactions on Aerospace and Electronic Systems*, vol. 40, no. 3, pp. 808–823, 2004.

[18] W. Whitacre and M. E. Campbell, "Decentralized geolocation and bias estimation for uninhabited aerial vehicles with articulating cameras," *Journal of guidance, control, and dynamics*, vol. 34, no. 2, pp. 564–573, 2011.

[19] E. Taghavi, R. Tharmarasa, T. Kirubarajan, Y. Bar-Shalom, and M. McDonald, "A practical bias estimation algorithm for multisensor-multitarget tracking," *IEEE Transactions on Aerospace and Electronic Systems*, vol. 52, no. 1, pp. 2–19, 2016.

[20] M. M. Mostafa, "Boresight calibration of integrated inertial/camera systems," in *Proc. International Symposium on Kinematic Systems in Geodesy, Geomatics and Navigation-KIS*, 2001, pp. 440–445.

[21] J. Skaloud and D. Lichti, "Rigorous approach to bore-sight self-calibration in airborne laser scanning," *ISPRS journal of photogrammetry and remote sensing*, vol. 61, no. 1, pp. 47–59, 2006.

[22] Z. Yang and S. Shen, "Monocular visual-inertial state estimation with online initialization and camera-imu extrinsic calibration," *IEEE Transactions on Automation Science and Engineering*, vol. 14, no. 1, pp. 39–51, 2016.

[23] J. Kelly and G. S. Sukhatme, "Visual-inertial sensor fusion: Localization, mapping and sensor-to-sensor self-calibration," *The International Journal of Robotics Research*, vol. 30, no. 1, pp. 56–79, 2011.

[24] T. Wang, Y. Zhang, Y. Zhang, G. Jiang, Z. Zhang, Y. Yu, and L. Dou, "Geometric calibration for the aerial line scanning camera gxfj," *Photogrammetric Engineering & Remote Sensing*, vol. 85, no. 9, pp. 643–658, 2019.

- [25] M. R. James, S. Robson, S. d'Oleire Oltmanns, and U. Niethammer, "Optimising uav topographic surveys processed with structure-from-motion: Ground control quality, quantity and bundle adjustment," *Geomorphology*, vol. 280, pp. 51–66, 2017.
- [26] E. Honkavaara, "In-flight camera calibration for direct georeferencing," *International Archives of Photogrammetry, Remote Sensing and Spatial Information Sciences*, vol. 35, no. B1, pp. 166–172, 2004.
- [27] A. Habib, T. Zhou, A. Masjedi, Z. Zhang, J. E. Flatt, and M. Crawford, "Boresight calibration of gnss/ins-assisted push-broom hyperspectral scanners on uav platforms," *IEEE Journal of Selected Topics in Applied Earth Observations and Remote Sensing*, vol. 11, no. 5, pp. 1734–1749, 2018.
- [28] C. Siying, M. Hongchao, Z. Yinchao, Z. Liang, X. Jixian, and C. He, "Boresight calibration of airborne lidar system without ground control points," *IEEE Geoscience and Remote Sensing Letters*, vol. 9, no. 1, pp. 85–89, 2011.
- [29] N. Yastikli, C. Toth, and D. Grejner-Brzezinska, "In-situ camera and boresight calibration with lidar data," in *Proc. The Fifth International Symposium on Mobile Mapping Technology, MMT*, vol. 7. Citeseer, 2007.
- [30] M. Li and A. I. Mourikis, "Online temporal calibration for camera–imu systems: Theory and algorithms," *The International Journal of Robotics Research*, vol. 33, no. 7, pp. 947–964, 2014.
- [31] E. S. Jones and S. Soatto, "Visual-inertial navigation, mapping and localization: A scalable real-time causal approach," *The International Journal of Robotics Research*, vol. 30, no. 4, pp. 407–430, 2011.
- [32] F. M. Mirzaei and S. I. Roumeliotis, "A kalman filter-based algorithm for imu-camera calibration: Observability analysis and performance evaluation," *IEEE transactions on robotics*, vol. 24, no. 5, pp. 1143–1156, 2008.
- [33] M. Arbabmir and M. Ebrahimi, "Visual–inertial state estimation with camera and camera–imu calibration," *Robotics and Autonomous Systems*, vol. 120, p. 103249, 2019.
- [34] T. Kailath, *Linear systems*. Prentice-Hall Englewood Cliffs, NJ, 1980, vol. 156.
- [35] P. Müller and H. Weber, "Analysis and optimization of certain qualities of controllability and observability for linear dynamical systems," *Automatica*, vol. 8, no. 3, pp. 237–246, 1972.
- [36] E. Gover and N. Krikorian, "Determinants and the volumes of parallelotopes and zonotopes," *Linear Algebra and its Applications*, vol. 433, no. 1, pp. 28–40, 2010.
- [37] J. A. Andersson, J. Gillis, G. Horn, J. B. Rawlings, and M. Diehl, "Casadi: a software framework for nonlinear optimization and optimal control," *Mathematical Programming Computation*, vol. 11, no. 1, pp. 1–36, 2019.
- [38] I. Pólik and T. Terlaky, "Interior point methods for nonlinear optimization," in *Nonlinear Optimization*. Springer, 2010, pp. 215–276.
- [39] J. E. Dennis, Jr and J. J. Moré, "Quasi-newton methods, motivation and theory," *SIAM Review*, vol. 19, no. 1, pp. 46–89, 1977.
- [40] D. C. Lay, S. R. Lay, and J. J. McDonald, *Linear algebra and its applications*. Pearson, 2016.



**Ziheng Cheng** received the B.Sc. degree in solid mechanics in 2012 and MSc degree in engineering mechanics in 2015 both from Xi'an Jiaotong University. He is currently pursuing his Ph.D. degree in School of Aerospace Engineering at Beijing Institute of technology. Her research interests include UAV swarm control and airborne image processing.



**Shaoming He** received the B.Sc. degree and the M.Sc. degree in aerospace engineering from Beijing Institute of Technology, Beijing, China, in 2013 and 2016, respectively, and the Ph.D. degree in aerospace engineering from Cranfield University, Cranfield, U.K., in 2019. He is currently a Professor with School of Aerospace Engineering, Beijing Institute of Technology and also a recognized teaching staff with School of Aerospace, Transport and Manufacturing, Cranfield University. His research interests include aerospace guidance, multitarget tracking and trajectory optimization.

Dr. He received the *Lord Kings Norton Medal* award from Cranfield University as the most outstanding doctoral student in 2020.



**Xiwen Yang** received her B.Sc. degree in flight vehicle design and engineering from Beijing Institute of technology, Beijing, China, in 2017. She is currently pursuing her Ph.D. degree in School of Aerospace Engineering at Beijing Institute of technology. Her research interests include multi-target tracking, information fusion, and cooperative target tracking.